



Contents lists available at ScienceDirect

Journal of the Mechanics and Physics of Solids

journal homepage: www.elsevier.com/locate/jmps

Interface toughening in multilayered systems through compliant dissipative interlayers

S. Dépinoy^{a,*}, F. Strepenne^b, T.J. Massart^c, S. Godet^a, T. Pardoen^b^a4MAT, Materials Engineering, Characterization, Processing and Recycling, Université Libre de Bruxelles, 50 Avenue FD Roosevelt, CP194/03, B-1050 Brussels, Belgium^bInstitute of Mechanics, Materials and Civil Engineering, UCLouvain, Place Sainte Barbe 2, 1348 Louvain-la-Neuve, Belgium^cBATir, Building, Architecture and Town Planning Department, Université Libre de Bruxelles, 50 Avenue FD Roosevelt, CP 194/02, B-1050 Brussels, Belgium

ARTICLE INFO

Article history:

Received 20 February 2019

Revised 25 April 2019

Accepted 18 May 2019

Available online 19 May 2019

Keywords:

Interface toughness

Multilayer

Finite element modeling

Wedge-opening test

Plastic dissipation

ABSTRACT

The effect on an interlayer on the toughness of an interface between a ductile thin film and an elastic substrate is investigated by finite element modeling and assessed towards experimental measurements. The model is based on an asymptotic K -field formulation relying on cohesive zone elements to simulate the fracture process. A compliant interlayer tends to increase the interface toughness by promoting plastic dissipation in the thin layer. Additional toughening can result from the development of plastic strains in the interlayer. The magnitude of these two toughening mechanisms depends on the film thickness, among other parameters. The model predictions are confirmed by comparison with wedge-opening test data performed on a multilayer composed of a thin Cu layer and a polymer interlayer embedded between two stainless steel substrates. These findings lay the foundation for the design of tougher multilayers and provide a critical assessment of experimental protocols for interface toughness measurements requiring the bonding of a dummy substrate, such as used for DCB or four point bending tests.

© 2019 Elsevier Ltd. All rights reserved.

1. Introduction

Multilayer materials consist of a stack of layers made of different materials with thickness typically ranging from several nanometers to several hundreds of micrometers. This broad definition encompasses a very wide range of structures and applications, from composite materials used in the aeronautic industry to microelectromechanical systems (MEMS).

A key parameter for the structural integrity of multilayers is the interface toughness G_c , usually quantified by the steady-state critical energy release rate G_{ss} associated to the propagation of a crack along an interface. This value is not only a function of the work of adhesion G_0 but also of other sources of dissipation, mainly plastic (or viscoplastic) dissipation, in the surrounding layers, e.g., (Tvergaard and Hutchinson, 1994). Hence, it is not always easy to predetermine if an interface will be “weak” based on physico-chemical arguments only. There are two approaches for interface toughening. The first one involves a modification of the interface itself, for instance through the generation of microstructural gradients within the layers surrounding the interface under concern (e.g., entanglement of polymer networks (Brown, 1991)), mechanical interlocking (Kim et al., 2010; Larsson et al., 2005), crack arrest patterns (Maloney and Fleck, 2019) or complex interface

* Corresponding author.

E-mail addresses: sdepinoy@gmail.com, sylvain.depinoy@ulb.ac.be (S. Dépinoy).

morphology (Cordisco et al., 2016). While efficient, these techniques are restrictive as they imply a complex deformation and fracture process or can be used only for specific materials. The second approach involves the engineering of multilayers making optimum use of plastic dissipation. As an example, Bertholet et al., 2007 proposed for an application in molecular bonding the introduction of a ductile interlayer next to a weak interface, following the generic configuration shown in Fig. 1. The role of this interlayer is only to deform plastically during the crack propagation at the interface between the thin layer and the substrate, thus improving the overall toughness. Bertholet et al., 2007 exclusively investigated this kind of configuration for a thin layer and a substrate made of an identical elastic material and a ductile interlayer with elastic properties identical to those of the other layers. For such case, the interface gets tougher as the thickness of the thin layer and of the interlayer decreases and increases, respectively. This is related to an increase in the magnitude of the plastic strains and plastic zone size in the interlayer. Other examples of a similar strategy exist in microelectronics (Dauskardt et al., 1998; Lane et al., 2000b, 2000a; Matsuda et al., 2014).

The system shown in Fig. 1 has other applications in which the interlayer is generally not introduced on purpose. When testing the adhesion of thin films on a substrate, the use of test configurations such as double cantilever beam (DCB) or four point bending require the bonding of an extra substrate (sometimes called “dummy substrate” or “superstrate”) in order to allow storing enough elastic energy to drive the cracking process along the interface (e.g., Dupont et al., 2013; Gandhi et al., 2007; Huang et al., 2005; Hughey et al., 2004; Kim et al., 2012a, 2012b; Ključar et al., 2015; Lee et al., 2012; Lemonds et al., 2002). The glue then acts as an interlayer which might dissipate energy that is extrinsic to the true toughness of the interface. This effect will be investigated in the present study through the proposed application/assessment, and could potentially impact a vast range of measurements performed in experimental labs throughout the world. Another example is given by polymer coatings deposited on anodized or ceramic protected substrates, for instance painting on anodized aluminum. In such case, a crack running at the interface between the substrate and the hard coating might lead to plastic dissipation in the polymer as well (this is a case where there is no extra substrate).

The present paper further investigates the effect of dissipative interlayers on enhancing interface toughness for a broad range of mechanical properties and dimensions. More precisely, the objective is to unravel the effect of the elastic behavior, yield strength and thickness of both layers (see Fig. 1) on the interface toughness based on a finite element framework. To this aim, a model based on the earlier works of Tvergaard and Hutchinson (1996, 1994, 1993, 1992) has been developed, referred to as the K -field model. Computations are performed under small scale yielding (SSY) conditions with an applied far-field displacement corresponding to a mode I remote energy release rate G using the usual linear elastic fracture mechanics (LEFM) relationships. The crack advance at the interface is simulated by a traction-separation law identified by a work of separation G_0 and a strength σ_c . Steady-state crack propagation occurs for $G = G_{SS}$ that is identified with the interface toughness G_c . The determination of the amplitude of the plastic dissipation $\varphi = G_{SS} - G_0$ is therefore straightforward and its dependency to various parameters can be directly investigated. The toughening effect related to the presence of the interlayer is assessed by performing similar simulations for a monolayer system (i.e., without interlayer).

For the sake of validation, the particular effect of the thickness of a ductile layer (1) (see Fig. 1) bonded to a compliant ductile interlayer (2) will be assessed for the specific case of a Cu coating (ductile layer (1) here) deposited on steel and bonded with a glue (interlayer (2)) to another steel substrate. A modified wedge opening test procedure involving the measurement of the out-of-plane displacement profile of the arm of the specimen was developed to characterize the interface toughness. One of the difficulties is related to the presence of internal stresses in the Cu layer.

The outline of the paper is the following. The experimental procedures for specimen preparation, the wedge opening test and the determination of the residual stresses are described in Section 2. Section 3 presents the K -field formalism used in the numerical simulations, along with the constitutive relationships and numerical methods. The limits of the model are also briefly discussed. The results of the parametric study are presented and discussed in Section 4, and the experimental results are discussed and compared with the numerical simulations in Section 5. Potential applications based on the numerical and experimental results are briefly discussed in the concluding section.

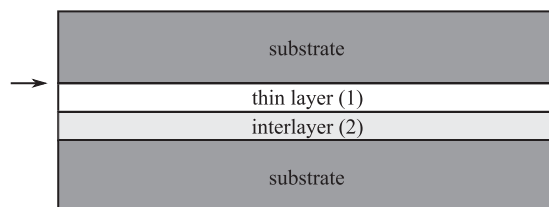


Fig. 1. Schematic drawings of the multilayer system involving a dissipative interlayer. The arrow represents the interface of interest.

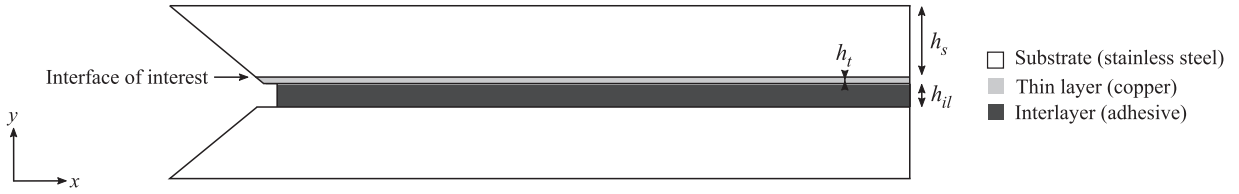


Fig. 2. Schematic representation of the tested multilayer system .

Table 1

Number of measurements for each specimen.

h_t (μm)	0.5	1	1.5	2	2.5
Pressure (Pa)	0.45	0.47	0.58	0.62	0.58
Number of measurements	14	14	12	4	12

2. Experimental protocol

2.1. Wedge opening tests

2.1.1. Specimen preparation

Wedge opening tests were performed on $10 \times 70 \times 0.4 \text{ mm}^3$ multilayered specimens as represented in Fig. 2. Copper deposition was performed on square $115 \times 115 \times 0.4 \text{ mm}^3$ stainless steel plates. Prior to the deposition process, the substrate was first cleaned in an ultrasonic bath with Methyl Acetate. The substrate was then introduced in the deposition chamber, where it underwent an ionic etching using a pulsed DC current source at 1.5 A to remove the residual oxide layer or other contaminants. The deposition chamber was then put under high vacuum (lower than 10^{-2} Pa), and the copper coating deposited under Argon atmosphere at a pressure ranging from 0.45 to 0.6 Pa. The generator used to induce the plasma was an Advanced Energy Pinnacle plus +10 kW. The target diameter was equal to 150 mm and the distance with the substrate was 70 mm. The deposition was performed under DC current at an intensity of 0.5 A. The coated plate was subsequently cut at proper dimensions, and the upper substrate was bonded to the Cu layer using a cyanoacrylate adhesive. The adhesive was applied with a brush in order to obtain a thickness as uniform as possible. The two parts were then pressed together for at least 12 h. Finally, a groove was made on the lower and upper substrates to facilitate the wedge insertion.

No pre-crack is inserted during the processing of the multilayer, thus the crack is susceptible to propagate along any of the three possible interfaces. Crack always follows the path offering the least resistance against propagation, thus crack propagation along the copper/stainless steel interface can be enforced by ensuring that this interface is weaker than the two other interfaces (i.e., on each side of the adhesive). The preparation of these two interfaces prior to the application of the adhesive is therefore very important and was made as follows. The Cu film was rinsed with norvanol (83.5% ethanol, 2.5% ether, 14% water) and dried with air. The roughness of the upper substrate was increased using SiC abrasive paper, then cleaned with demineralized water, rinsed with norvanol and dried with hot air. Specimens were produced with five different thicknesses of the Cu layer h_t , ranging from 500 nm to 2.5 μm , with their corresponding deposition pressure summarized in Table 1. The thickness of the cyanoacrylate adhesive h_{il} was not measured but is estimated to be around 50 μm .

2.1.2. Interface fracture tests

The mode I fracture energy was obtained using an adapted wedge opening test procedure, schematized in Fig. 3a. The crack was advanced by inserting a razor blade of thickness $D = 100 \mu\text{m}$ between the substrates arms. For a symmetric specimen, the adhesive fracture energy G_c is derived from the crack length a such that:

$$G_c = \frac{3E_s h_a^3 D^2}{16a^4 (1 - \nu_s^2)} \left(1 + 0.674 \frac{h_a}{a} \right)^2, \quad (1)$$

where E_s , ν_s and h_a are the Young's modulus, the Poisson ratio and the thickness of the arm, respectively. The corrective factor term $(1 + 0.674 h_a/a)^2$ takes into account the effect of the root rotation associated with the presence of shear stresses in the near crack tip region (Li et al., 2004). The experimental system depicted in Fig. 2 is not perfectly symmetric as the crack propagates between the copper film and the substrate. However, the thickness of the adhesive and of the copper film are negligible compared to the thickness h_s of the substrate and are not taken into account, such that $h_a = h_s = 0.4 \text{ mm}$.

Due to the corrective factor, Eq. (1) depends on the inverse of a sextic polynomial of a . Thus, the measurement of the crack length has to be as accurate and reliable as possible. In the case of transparent substrates, the crack length can be determined using optical methods, see (Bertholet et al., 2004) for instance. Such methods are obviously not adapted for non-transparent substrates as used here. Thus, an indirect procedure was defined based on the out-of-plane displacement profile $u_y(x)$ of the specimen, following the earlier work of Navarro et al. (2013), Bertholet et al. (2007) and Olbrechts et al.

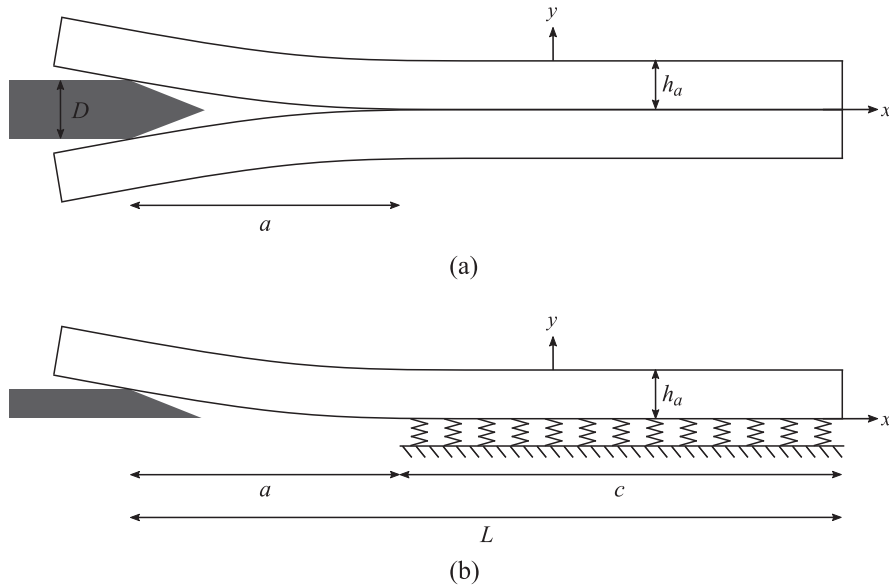


Fig. 3. Descriptions of (a) the wedge opening test configuration for a symmetric specimen and (b) a beam resting on an elastic foundation.

(2006). The relationship between $u_y(x)$ and a can be determined analytically by comparing one arm of the wedge opening test to a beam deformed by an imposed displacement at a distance a from the crack tip. In order to take into account the root-rotation, the formulation proposed by Kanninen (1973), based on an Euler-Bernoulli beam resting on a Winkler elastic foundation (Fig. 3b), was chosen. A beam of length L is attached to an elastic foundation over a length c (thus $L = c + a$). The analytical expression for $u_y(x) = f(a)$ for the x interval $(0, a)$, where $x = 0$ is the free end of the arm, is given by:

$$u_y(x) = \frac{3D}{h_a^3 \lambda^3 \phi} \left[\frac{\lambda^3 (x - a)^3}{3} + a \lambda^3 (x - a)^2 - A(a)(x - a) + B(a) \right], \quad (2)$$

where ϕ , λ , $A(a)$ and $B(a)$ are given in Appendix A.

The out-of-plane displacement profile was experimentally measured with a contact profilometer Veeco Dektak 50. A simple testing stage was designed to allow a precise positioning of the wedge within the specimen and the measurement of the vertical displacement field under the profilometer. The crack length was then retrieved by fitting Eq. (2) with the measured displacement profile using a least square method. This methodology was first validated on an ideal system of two silicon wafers joined by molecular bonding. Such system is transparent to IR radiation, allowing a direct, optical measurement of a (Bertholet et al., 2004). The deviation between the crack lengths as measured by the two methodologies was found to be around 4% (Strepenne, 2010).

The wedge opening tests were conducted as follows. Measurements of the displacement profile were performed immediately after wedge insertion. Several displacement profiles, corresponding to different crack lengths, were measured for each specimen. As already stated, the interface subjected to debonding cannot be controlled, and the validity of each measurement must be assessed at the end of the test by analyzing the fractured specimen. Measurements that did not correspond to crack propagation between the Cu layer and the steel substrate were discarded. The number of measurements taken into account for the determination of G_c for all studied specimens is given in Table 1.

2.2. Residual stresses in the Cu layer

Residual stresses in thin layers arise from differences in thermal expansion coefficients or in lattice parameters between the substrate and the film, from the growth of the layer or from microstructure evolution effects (Freund and Suresh, 2004). These residual stresses can depend on film thickness and can have a strong effect on the resistance to crack propagation along the interface. Indeed, tensile stresses parallel to the interface lead to lower apparent toughness, while compressive stresses lead to an effective toughening (Strohband and Dauskardt, 2003; Tvergaard, 2003; Tvergaard and Hutchinson, 1996). It is therefore important to characterize the magnitude of these stresses to assess their influence on the measured interface toughness.

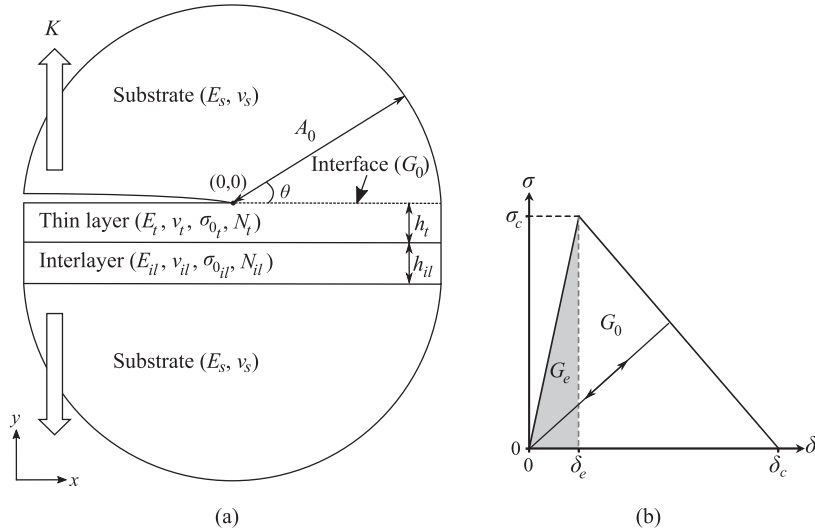
The average residual stress in the Cu layers was determined using the Stoney method (Stoney, 1909). Assuming that the film is much thinner than the substrate, the curvature of the substrate is related to the residual stress σ_R in the coating by:

$$\sigma_R = \frac{E_s h_s^2}{6(1 - \nu_s) h_f} (C - C_0), \quad (3)$$

Table 2

Cu deposition conditions of the specimen used for the measurements of residual stresses.

h_t (μm)		0.25	0.5	1	1.5	2	2.5
Pressure (Pa)	Batch 1	0.45	0.45	0.54			
	Batch 2		0.65	0.64	0.67	0.67	0.67
	Batch 3	0.53	0.57	0.57	0.537	0.53	0.53

**Fig. 4.** (a) Configuration of the asymptotic K-field model, (b) Interface bi-triangular traction-separation law.

where C_0 and C correspond to the curvature of the substrate before and after deposition, respectively. Curvatures were determined here using a Veeco Dektak 50 profilometer.

Measurements could not be performed directly on steel substrates which are not sufficiently planar, instead, silicon wafers ($E_s/(1-\nu_s) = 180$ GPa and $h_s = 380$ μm) coated with a 0.3 μm layer of stainless steel were used to mimic as well as possible the real system. Thus, in Eq. (3), C_0 corresponds to the curvature of the silicon + stainless steel system. Measurements were done on Cu films from three different batches which only differed by the deposition pressure, as shown in Table 2.

Using Eqs. (1) to (3), this experimental protocol was used to retrieve the interface toughness of the considered multilayer system as a function of the thickness of the layer, along with the magnitude of the residual stresses in the thin layer. These results are reported in Section 5 and compared to the numerical trends.

3. Computational model

3.1. Generic K-field formalism

The geometry used to study crack propagation is shown in Fig. 4a. It is based on the seminal work by Tvergaard and Hutchinson on the toughness of ductile adhesive joints (Tvergaard and Hutchinson, 1994). Two layers, referred to in the following as the thin layer and the interlayer and defined by their respective elastoplastic properties and thicknesses, are embedded between two identical semi-circular elastic substrates of radius A_0 . An interface crack is inserted between the thin layer and the upper substrate along $x < 0$ and $y = 0$. The fracture process takes place along the line $x > 0$ and $y = 0$, and is simulated by a traction-separation law characterized by the work of fracture G_0 and the fracture strength σ_c (Fig. 4b). Assuming that $A_0 \gg (h_t + h_{il})$, the crack can be considered as semi-infinite and the overall system respects the small-scale yielding conditions. Crack growth is therefore induced by remotely applying a symmetrical mode I, plane strain displacement field at the boundary of the model, with the initial crack tip located at the origin of the cartesian reference system. The amplitude of the displacement field is controlled by the magnitude of the stress intensity factor K . Irwin's relationship between K and the energy release rate G for mode I under plane strain conditions is given by

$$K = \left[\frac{E_s G}{(1 - \nu_s^2)} \right]^{1/2}. \quad (4)$$

In this configuration, G can be considered as a remote energy release rate and is identified with the crack growth resistance G_c if the crack propagates. The crack resistance curve $G(\Delta a)$, where Δa is the crack extension, can then be easily retrieved, as increasing the displacements at the model boundary is tantamount to increasing G . Steady-state crack propagation occurs for $G = G_{ss}$, where $G_{ss} = G_0 + \varphi$, φ being the amount of energy dissipated through plastic deformation in the thin layer and interlayer.

3.2. Constitutive laws

3.2.1. Traction-separation law of the interface

A bi-triangular damage interface material law implemented in the finite element code SAMCEF, as schematized in Fig. 4b, characterizes the separation of the interface, i.e., the crack extension process. More information about the constitutive equations describing the traction-separation law can be found in Ladevèze et al. (1998) and Bruyneel et al. (2014).

A linear elastic behavior defined by the elastic displacement jump δ_e and the critical stress σ_c is assumed, corresponding to an elastic work per unit area G_e (light grey area in Fig. 4b). For $\delta > \delta_e$, the stress decreases with the development of damage, i.e., any unloading occurs with a decreasing secant stiffness toward the origin of the stress-strain response. Complete fracture occurs when the displacement jump reaches a critical value δ_c . The fracture process corresponds to the total area under the curve in Fig. 4b and is thus defined by a work per unit area such that

$$G_0 = \frac{\sigma_c \delta_c}{2}. \quad (5)$$

The asymmetry introduced by the positioning of the crack, by the different properties of the different materials and by the occurrence of plastic deformation can induce tangential displacements of the crack faces, even if an overall pure mode I is applied to the system (Tvergaard and Hutchinson, 1994). Thus, the traction-separation law must be defined within a mixed-mode setting. For reasons of simplicity, identical parameters δ_e , δ_c and σ_c (and therefore G_0) were taken for both the normal (mode I) and tangential (mode II) contributions. The displacement jumps are coupled in such a way that fracture occurs when a nondimensional crack separation indicator $\bar{\delta}$ reaches 1, with $\bar{\delta}$ defined as:

$$\bar{\delta} = \left[\left(\frac{\delta_I}{\delta_c} \right)^2 + \left(\frac{\delta_{II}}{\delta_c} \right)^2 \right]^{1/2}, \quad (6)$$

where the indices I and II represent the normal and tangential components, respectively.

3.2.2. Properties of the ductile layers and of the elastic substrates

The substrates are assumed to be isotropic linear, defined by Young's modulus E_s and Poisson ratio ν_s . The elastic behavior of the layers is isotropic linear and defined by the Young's modulus E_t and E_{il} and Poisson ratio ν_t and ν_{il} , respectively. Plasticity is modeled using the isotropic J_2 flow theory. The effective stress is defined classically as $\sigma_e = \sqrt{(3/2)s_{ij}s_{ij}}$, where $s_{ij} = \sigma_{ij} - (1/3)\sigma_{kk}\delta_{ij}$ are the components of the deviatoric stress tensor with σ_{ij} the components of the Cauchy stress tensor and δ_{ij} the Kronecker delta. The effective plastic strain is computed as $\bar{\varepsilon}_p = \sqrt{(2/3)\varepsilon_{ij}^p\varepsilon_{ij}^p}$, where ε_{ij}^p are the components of the plastic strain tensor. σ_e and $\bar{\varepsilon}_p$ are related to each other through the following hardening law (Tvergaard and Hutchinson, 1992):

$$\sigma_{ei} = \sigma_{0i} \left(1 + \frac{E_i \bar{\varepsilon}_p}{\sigma_{0i}} \right)^{N_i}, \quad (7)$$

where σ_0 is the yield stress prescribing the onset of plasticity and N is the strain hardening exponent. Indices i describe the behavior of the thin layer ($i=t$) and of the interlayer ($i=il$).

3.3. Selection of material parameters for the parametric study

The overall steady-state interface toughness is characterized by 16 material and geometrical parameters such that

$$G_{ss} = F(E_t, \nu_t, \sigma_{0t}, N_t, h_t, E_{il}, \nu_{il}, \sigma_{0il}, N_{il}, h_{il}, E_s, \nu_s, \delta_e, \delta_c, \sigma_c, A_0). \quad (8)$$

In principle, A_0 should not enter the variables in Eq. (8) in the context of a small-scale yielding framework. Indeed, once A_0 is large enough to ensure small-scale yielding conditions, further increase of this parameter should not impact the overall value of the interface toughness. However, it has been found that this is not true in this study for reasons explained in Section 4.2.2. Eq. (8) can be nondimensionalized in the following form:

$$\frac{G_{ss}}{G_0} = F \left(\frac{\sigma_{0t}}{E_t}, N_t, \frac{\sigma_{0il}}{E_{il}}, N_{il}, \frac{E_s}{E_t}, \frac{E_t}{E_{il}}, \nu_s, \nu_t, \nu_{il}, \frac{h_t}{R_0}, \frac{h_{il}}{R_0}, \frac{A_0}{R_0}, \frac{\sigma_c}{\sigma_{0t}}, \frac{\delta_e}{\delta_c} \right), \quad (9)$$

where R_0 is a reference length corresponding to an estimate of the plastic zone size inside the thin layer at $G=G_0$ for $h_t \gg R_0$, as proposed by [Tvergaard and Hutchinson \(1993\)](#):

$$R_0 = \frac{2}{3\pi(1-\beta^2)} \left[\frac{(1-\nu_s^2)}{E_s} + \frac{(1-\nu_t^2)}{E_t} \right]^{-1} \frac{G_0}{\sigma_{0t}^2}, \quad (10)$$

where β is the second Dundurs' mismatch parameter

$$\beta = \frac{1}{2} \frac{\mu_t(1-2\nu_s) - \mu_s(1-2\nu_t)}{\mu_t(1-\nu_s) + \mu_s(1-\nu_t)}, \quad (11)$$

and where μ_t and μ_s are the shear moduli of the thin layer and of the substrate, respectively, such that $\mu = E/(2+2\nu)$. In the absence of elastic mismatch between the substrate and the thin layer, [Eq. \(10\)](#) reduces to

$$R_0 = \frac{1}{3\pi(1-\nu_s^2)} \frac{E_s G_0}{\sigma_{0t}^2}. \quad (12)$$

Particularizing the study to the context of metallic thin films, constant values of $\nu_t=0.3$, $\sigma_{0t}/E_t=0.003$ and $N_t=0.1$ were considered. Thus, the only parameter describing the thin layer that will be systematically varied is the thickness, h_t/R_0 , with a value between 0.25 and 3. The parameters associated with the interlayer, E_t/E_{il} , h_{il}/R_0 and σ_{0il}/E_{il} are varied. The other parameters that were fixed are $N_{il}=0.1$ and $\nu_{il}=0.3$. Depending on the selected value of σ_{0il}/E_{il} , the numerical simulations can be separated in two categories. The “elastic interlayer” corresponds to $\sigma_{0il}/E_{il} \rightarrow \infty$. The “elastoplastic interlayer” refers to the simulations in which plasticity develops in the interlayer during the crack advance process. The elastic case can thus be considered as an asymptotic value of the elastoplastic case. Finally, the last parameters that are varied involve the elastic mismatch between the substrate and the thin layer E_s/E_t and the interface strength σ_c/σ_{0t} . The three remaining material parameters were kept constant: the Poisson ratio of the substrate $\nu_s=0.3$, such that the substrates, the thin layer and the interlayer have the same ν . The elastic displacement jump of the interface is known to be of secondary importance and was set to $\delta_e/\delta_c=0.01$, since a larger value would delay damage towards higher displacements. Finally, A_0/R_0 was taken equal to 1250.

In order to evaluate the effect of the interlayer on the overall toughness, additional simulations were performed without the interlayer to obtain a reference value of G_{ss}/G_0 . In this further case referred to as the “monolayer case”, the steady-state interface toughness is defined by nine non-dimensional parameters such that

$$\frac{G_{ss}(\text{monolayer})}{G_0} = F \left(\frac{\sigma_{0t}}{E_t}, N_t, \frac{E_s}{E_t}, \nu_s, \nu_t, \frac{h_t}{R_0}, \frac{A_0}{R_0}, \frac{\sigma_c}{\sigma_{0t}}, \frac{\delta_e}{\delta_c} \right). \quad (13)$$

For a given set of non-dimensional parameters shown in [Eq. \(13\)](#), the change in interface toughness related to the introduction of an elastic interlayer, denoted $\Delta\varphi_a/G_0$, is retrieved by subtracting the toughness for the monolayer case from the one for the elastic interlayer case. Similarly, the change in toughness resulting from the plasticity in the interlayer, noted $\Delta\varphi_b/G_0$, is the difference between the toughness of the elastoplastic case and the one of the elastic case, where the only variable in [Eq. \(9\)](#) is σ_{0il}/E_{il} . Thus, $\Delta\varphi_a/G_0=0$ and $\Delta\varphi_b/G_0=0$ means that no extra dissipation of energy takes place between the considered cases.

3.4. Finite element model

[Fig. 5](#) shows the typical finite element mesh used for the simulations, made of quadrilateral elements with quadratic interpolation functions. The mesh is highly refined at the initial crack tip with square elements of size d_0 repeated over the x -axis along a length B_0 . These elements are repeated in the y -direction up to $y=-h_t-(R_0/2)$, followed by rectangular elements of dimensions $(d_0 \times 10 d_0)$ up to $y=-h_t-h_{il}$. Thus, the thin layer is entirely meshed using square elements, while the interlayer is discretized by square elements at the vicinity of the interface with the thin layer, and by rectangular elements otherwise. The size of the zone of interest, B_0 , was taken of the same order of magnitude as R_0 , and the maximum dimension of the system, A_0 , is 1250 times R_0 (i.e., more than 100 times h_t+h_{il}). The fracture process at the interface is simulated using zero-thickness cohesive zone elements. A mesh resolution of R_0/d_0 equal to ~ 80 was selected. This leads to selecting δ_c/d_0 as varying between 0.6 and 1.4, depending on E_s/E_t and on σ_c/σ_{0t} .

The displacement field (u_x, u_y) corresponding to a mode I plane strain loading is applied on the outer nodes of the half-disks of the model. For the upper half-disk, the displacement distribution is given by

$$u_x = \frac{K}{2\mu_s} \left(\frac{A_0}{2\pi} \right)^{1/2} \cos \frac{\theta}{2} \left[(3 - 4\nu_s) - 1 + 2\sin^2 \frac{\theta}{2} \right], \quad (14)$$

$$u_y = \frac{K}{2\mu_s} \left(\frac{A_0}{2\pi} \right)^{1/2} \sin \frac{\theta}{2} \left[(3 - 4\nu_s) + 1 - 2\cos^2 \frac{\theta}{2} \right], \quad (15)$$

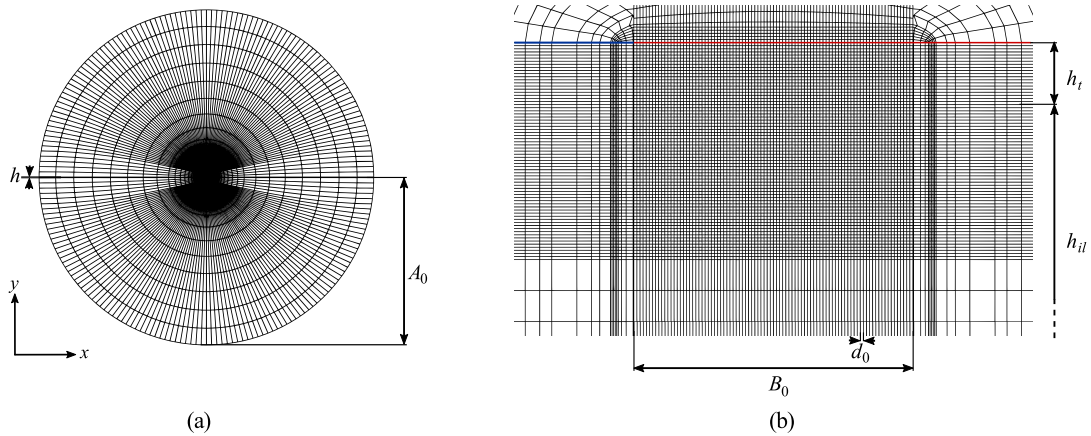


Fig. 5. Finite element mesh, (a) full mesh, (b) refined mesh at the fracture process zone ($h_t/R_0 = 0.25$, $h_{il}/R_0 = 2$). The blue and red lines symbolize the pre-crack and the interface, respectively. (For interpretation of the references to color in this figure legend, the reader is referred to the web version of this article.)

where θ is the angle between the crack plane and the direction defined by the line joining the crack tip to the outer node (see Fig. 4a). Displacements of the lower half-disk are symmetrical with respect to the x -axis.

Calculations are performed under plane strain conditions using the 2nd Piola–Kirchhoff stress and Green strain. Non-linear static analyses are performed by linearly increasing K using a Newton–Raphson solution scheme implemented in the code SAMCEF (MECANO solver). An adaptive time stepping is used, and a steady-state crack growth regime is reached with very small increments of K , resulting in crack advance for a virtually constant value of K . When steady-state crack growth is not achieved for $\Delta a = B_0$, G_{ss} is taken as the value of G for $\Delta a/R_0 = 1$. In such cases, G does not rigorously correspond to G_{ss} and is actually lower than the real value of G_{ss} .

Due to the large differences between the yield strength of the thin layer and of the interlayer, a similar magnitude of plastic strains in these two layers does not lead to the same amount of energy dissipated. Thus, interpretations based on the graphical representation of plastic strains distributions can be misleading, and the analysis is more direct when the results are given in terms of plastic energy dissipation. The total plastic energy dissipated per unit volume in each layer, φ_{v_i} , where $i = t$ describes the thin layer and $i = il$ the interlayer, can be computed as

$$\varphi_{v_i}(\bar{\varepsilon}_p) = \int \sigma_{e_i} d\bar{\varepsilon}_p(\bar{\varepsilon}_p). \quad (16)$$

For the strain hardening law (7), Eq. (16) becomes:

$$\varphi_{v_i}(\bar{\varepsilon}_p) = \sigma_{0_i}^2 \frac{(1 + E_i \bar{\varepsilon}_p / \sigma_{0_i})^{N_i+1} - 1}{E_i (N_i + 1)}. \quad (17)$$

3.5. Limitations of the model

The present model aims at identifying general trends which may not be fully representative of real structures. Indeed, in real structures of finite size, the stress field deviates significantly from the K -field since the K -dominated zone A_0 in such structures is rather small, typically a few percents of the crack length (Charalambides et al., 1992). This is especially relevant here since it is assumed that the K -dominated zone encompasses the thin layer and the interlayer, which may not be true experimentally. Furthermore, it will be shown in Section 4.2.2 that A_0 has an impact on the final value of G_{ss} .

In addition, two important features intrinsic to thin metallic layers are not considered in this study. As stated in Section 2, thin metallic layers exhibit residual stresses with a magnitude that usually depends on film thickness. These residual stresses may play a prominent role when it comes to the determination of the interface toughness, to the point that debonding due to such residual stresses may occur in certain circumstances without any externally added loading (He et al., 1997). This is even a possible method to determine interface toughness by estimating a critical thickness above which delamination occurs (Argon et al., 1989). The effect of residual stresses in multilayers is out of the scope of this study, and the reader is referred to Tvergaard (2003) and Tvergaard and Hutchinson (1996) for more information. Finally, it is known that the yield strength of metallic films tends to evolve with thickness: a thinner film will exhibit a higher yield strength (Freund and Suresh, 2004). This is a direct consequence of the evolution of the grain size with film thickness. Such considerations are not taken into account in our model.

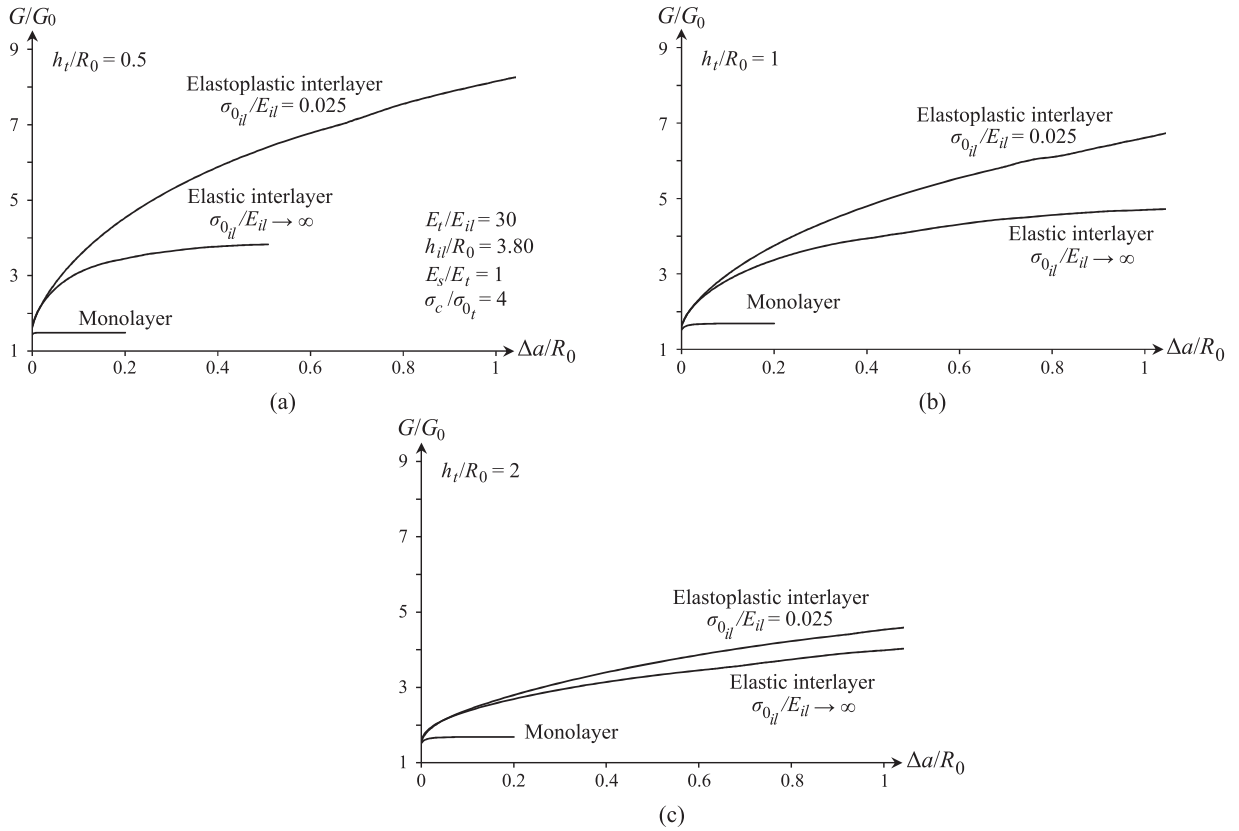


Fig. 6. Crack growth resistance curves for the monolayer case, the elastic interlayer case ($\sigma_{0_{il}}/E_{il} \rightarrow \infty$) and the plastic interlayer case ($\sigma_{0_{il}}/E_{il} = 0.025$) for (a) $h_t/R_0 = 0.5$, (b) $h_t/R_0 = 1$, (c) $h_t/R_0 = 2$.

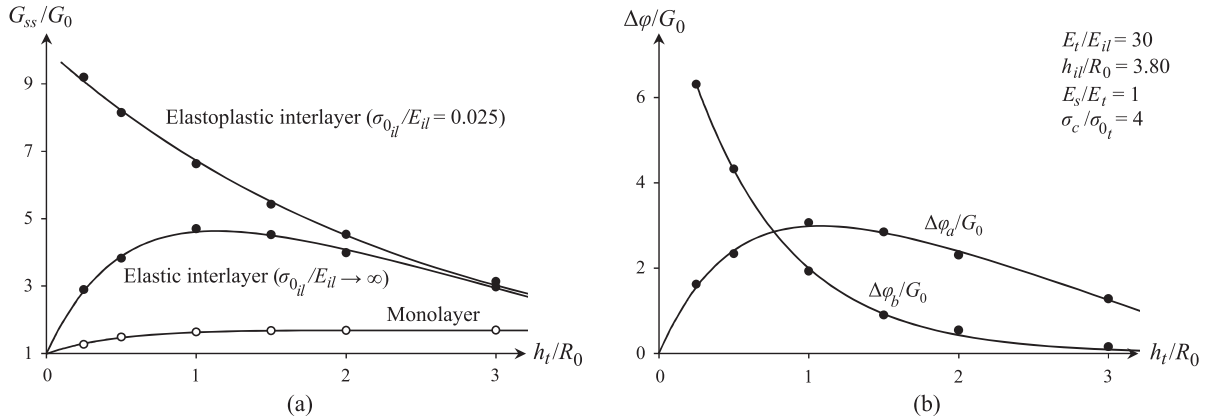


Fig. 7. (a) Variation of the overall interface toughness with h_t/R_0 for the three investigated cases: monolayer alone, elastic interlayer and plastic interlayer (b) Corresponding evolution of the extra dissipation due to the presence of an interlayer $\Delta\varphi_a/G_0$ and $\Delta\varphi_b/G_0$. Other parameters are $E_t/E_{il} = 30$, $h_{il}/R_0 = 3.80$, $E_s/E_t = 1$ and $\sigma_c/\sigma_{0_t} = 4$. Dots are the results from FE calculations and solid lines are guides for the eye.

4. Results and analysis of numerical simulations

4.1. Parametric study on the variation of the interface toughness

An example of predicted crack resistance curves for the monolayer case and for systems with an elastic or plastically deforming interlayer corresponding to different values of h_t/R_0 is given in Fig. 6. The interface toughness dependence on

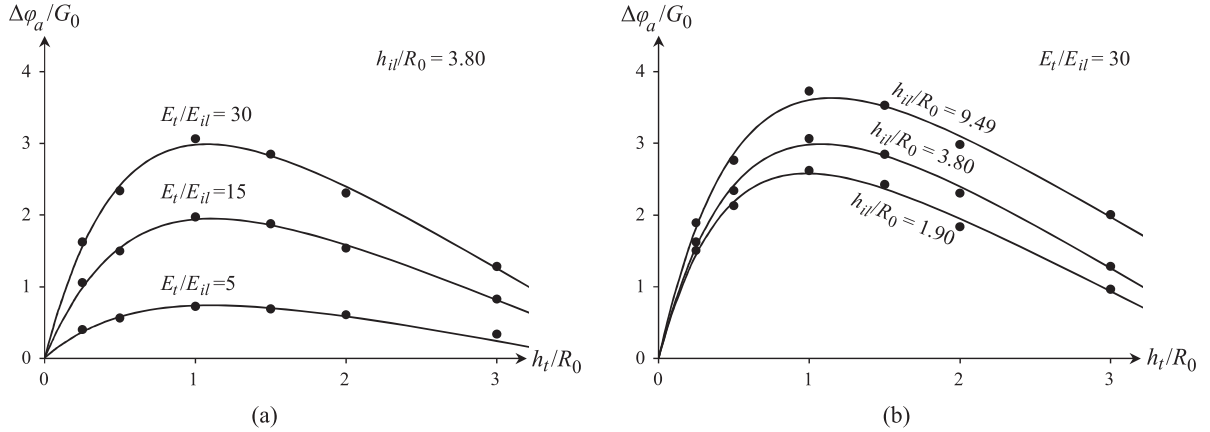


Fig. 8. Effect of (a) E_t/E_{il} and (b) h_{il}/R_0 on the extra contribution to the interface toughness associated to the elastic deformation in the interlayer $\Delta\varphi_a/G_0$ as a function of h_t/R_0 . Other parameters are the ones from Fig. 7. Dots are the results from FE calculations and solid lines are guides for the eye.

h_t/R_0 is shown in Fig. 7a. The parameters selected for the simulations are $E_t/E_{il}=30$, $h_{il}/R_0=3.80$, $E_s/E_t=1$ and $\sigma_c/\sigma_{0t}=4$. Fig. 7b shows the corresponding evolution of $\Delta\varphi_a/G_0$ and $\Delta\varphi_b/G_0$ with h_t/R_0 .

The properties of the interlayer heavily affect the interface toughness evolution with h_t/R_0 . While the dependence of G_{ss}/G_0 on h_t/R_0 has already been reported for the monolayer case (Martiny et al., 2012; Tvergaard and Hutchinson, 1994) and, to some extent, for the plastic interlayer case (Bertholet et al., 2007; Wei and Hutchinson, 1999), the fact that an elastic interlayer can induce a significant toughening is a new finding. The next subsections aim at describing the evolution of the interface toughness with h_t/R_0 for the three studied cases, as well as its dependence on the investigated parameters. The general effect of E_s/E_t and σ_c/σ_{0t} is discussed in a fourth subsection.

4.1.1. Monolayer case

For the monolayer case, the toughness first increases with h_t/R_0 up to a maximum value. Further increasing h_t/R_0 has no effect on G_{ss}/G_0 . In Fig. 7, this condition is reached for $h_t/R_0 \sim 1$. This evolution of G_{ss}/G_0 with h_t/R_0 is well documented and has been the subject of numerous numerical (Martiny et al., 2012; Pardoën et al., 2005; Tvergaard and Hutchinson, 1996, 1994) and experimental (Ikeda et al., 2000; Kinloch and Shaw, 1981) studies. These mechanisms will be briefly summarized in Section 4.2.1, for comparison purposes.

4.1.2. Elastic interlayer

Two main observations can be made based on the results of Fig. 7 regarding the effect of an elastic interlayer on the interface toughness. First, it appears that the elastic case always exhibits a higher toughness compared to the monolayer case, i.e., $\Delta\varphi_a/G_0 > 0$. This has been proven true regardless of the choice of the parameters, as long as the interlayer is softer than the thin layer (i.e., $E_t/E_{il} > 1$). Indeed, while not shown here for brevity, calculations performed for $E_t/E_{il}=0.2$ always resulted in $\Delta\varphi_a/G_0=0$. Second, it appears that $\Delta\varphi_a/G_0$ is highly dependent on layer thickness: it first increases with h_t/R_0 up to a maximum value, followed by a decrease when further increasing h_t/R_0 . In Fig. 7, this maximum is reached for $h_t/R_0 \sim 1$. For large values of h_t/R_0 , $\Delta\varphi_a/G_0$ seems to converge towards 0. These results are at the core of the current study with impact in different practical or technologically relevant situations, and the particular mechanisms leading to this toughening will be further analyzed in Section 4.2.2.

Among the different studied parameters, E_t/E_{il} and h_{il}/R_0 were found to have an important effect on the dependence of $\Delta\varphi_a/G_0$ on h_t/R_0 , as illustrated in Fig. 8. It appears that $\Delta\varphi_a/G_0$ generally decreases with decreasing E_t/E_{il} , in a way that $\Delta\varphi_a/G_0(h_t/R_0) \rightarrow 0$ for $E_t/E_{il} \rightarrow 1$. Decreasing h_{il}/R_0 shifts $\Delta\varphi_a/G_0$ towards lower values, but this effect is less important than the impact of the elastic mismatch E_t/E_{il} .

4.1.3. Plastic interlayer

As shown in Fig. 7, $\Delta\varphi_b/G_0$ decreases with increasing h_t/R_0 . Above a critical value of the ratio h_t/R_0 , there is no significant toughening resulting from the plasticity in the interlayer. In Fig. 7, the critical non dimensional thickness is $h_t/R_0 \sim 3$.

Fig. 9 shows the effect of σ_{0il}/E_{il} and h_{il}/R_0 on the elastoplastic contribution $\Delta\varphi_b/G_0(h_t/R_0)$. Decreasing σ_{0il}/E_{il} leads to a general increase of $\Delta\varphi_b/G_0$, especially for low values of h_t/R_0 , and shifts the critical value of h_t/R_0 towards larger thickness. An increase in h_{il}/R_0 leads to a slight increase of $\Delta\varphi_b/G_0$ when $\sigma_{0il}/E_{il}=0.025$. While not shown there, it has been found that increasing h_{il}/R_0 has no effect when σ_{0il}/E_{il} is equal to 0.05.

These trends were already described and analyzed by Wei and Hutchinson (1999) and Bertholet et al. (2007) in simulations with an elastic thin layer and an elastoplastic interlayer. The mechanisms responsible for this toughening are discussed in Section 4.2.3.

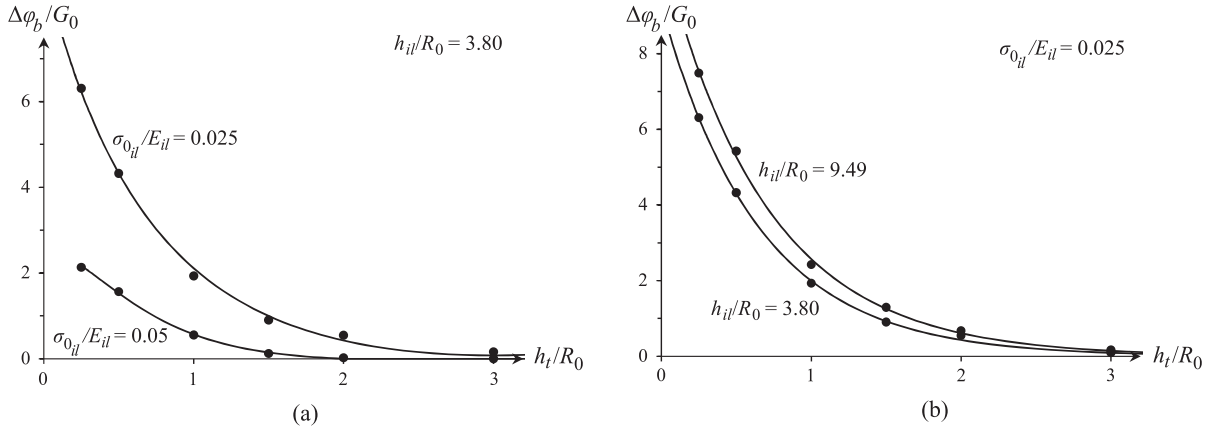


Fig. 9. Effect of (a) $\sigma_{0_{ii}}/E_{ii}$ and (b) h_{ii}/R_0 on the dependence of the extra dissipation due to a plastically deforming interlayer $\Delta\varphi_b/G_0$ on h_t/R_0 . Other parameters are the ones from Fig. 6. Dots are the results from FE calculations and solid lines are guides for the eye.

4.1.4. Effect of E_s/E_t and σ_c/σ_{0_t}

The effect of E_s/E_t and σ_c/σ_{0_t} on the interface toughness evolution with h_t/R_0 for all three cases (monolayer, elastic interlayer and elastoplastic interlayer) was investigated but is not described here. In summary, it showed that increasing these two parameters always leads to an increase of the interface toughness:

- For the monolayer case, it leads to a general increase of G_{ss}/G_0 , which reaches a constant value for larger h_t/R_0 . This is a well-known result as already reported by [Tvergaard and Hutchinson \(1996\)](#) for instance.
- For the elastic interlayer, it leads to a general increase of the extra dissipation $\Delta\varphi_a/G_0$ with a maximum in $\Delta\varphi_a/G_0$ reached for larger values of h_t/R_0 .
- For the plastic interlayer, it leads to a general increase of the extra dissipation $\Delta\varphi_b/G_0$, and shifts the critical h_t/R_0 towards higher values.

Furthermore, no coupling effect is found between E_s/E_t and σ_c/σ_{0_t} on the one hand, and E_t/E_{ii} , h_{ii}/R_0 and $\sigma_{0_{ii}}/E_{ii}$ on the other hand. The variation of the toughening effect associated to changes in E_s/E_t and σ_c/σ_{0_t} for each case will thus only be briefly explained in [Sections 4.2.1–4.2.3](#).

4.2. Toughening mechanisms

4.2.1. Monolayer case

The effect of h_t/R_0 on G_{ss}/G_0 for the monolayer case is first addressed, see also details in [Martiny et al. \(2012\)](#) and [Tvergaard and Hutchinson \(1996\)](#). [Fig. 10a](#) shows the evolution of the steady-state plastic energy dissipation zone as a function of h_t/R_0 .

Depending on h_t/R_0 , the steady state plastic energy dissipation zone can be divided into two different zones A and C, following the notations introduced by [Martiny et al. \(2012\)](#), which are represented on [Fig. 10b](#) for $h_t/R_0 = 0.5$. The first plastic dissipation zone PZA is located directly under the crack tip and is mainly the result of the normal stress field arising from the crack opening process. When this stress field interacts with the lower substrate (i.e., for low values of h_t/R_0), shear stresses develop at the thin layer/substrate interface which are responsible for the second plastic-dissipation zone PZC. Increasing h_t/R_0 first tends to increase the size of both zones. Above a certain value of h_t/R_0 , the size of the first zone keeps increasing while the size of the second zone decreases. Ultimately, there is no more interaction between the crack-tip stress field and the lower substrate: the secondary plastic zone vanishes and all the energy dissipation is due to crack-tip plasticity. Consequently, the energy dissipation becomes independent of h_t/R_0 .

Increasing the mismatch in elastic properties E_s/E_t and the interface strength σ_c/σ_{0_t} leads to more crack-tip plasticity, thus increasing the plastic dissipation and shifting the toughness plateau towards larger values of h_t/R_0 .

4.2.2. Interface toughening associated to an elastic interlayer

The effect with an elastic interlayer of h_t/R_0 , E_t/E_{ii} and h_{ii}/R_0 on the steady-state plastic zones at $G = G_{ss}$ can be analyzed based on [Fig. 11](#). When compared to [Fig. 10](#), the presence of an elastic interlayer has a strong influence on the plastic zone shape and extension in the thin layer. Up to four different plastic energy dissipation zones can be identified in [Fig. 11](#), as schematized in [Fig. 12](#). These four plastic zones are located:

- under the crack plane, near the crack tip (PZ1);
- at the interface between the thin layer and interlayer, ahead of the crack tip (PZ2);
- at the interface between the thin layer and interlayer, behind the crack tip (PZ3);

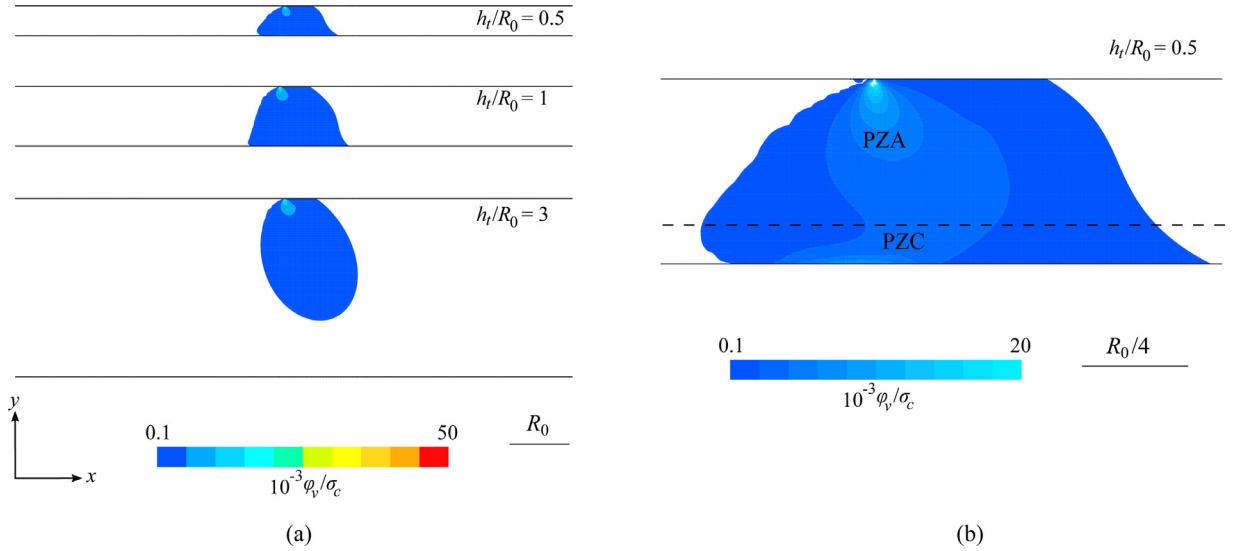


Fig. 10. (a) Steady-state plastic dissipation zone in the thin layer as a function of h_t/R_0 for the monolayer case. The corresponding evolution of the interface toughness is shown in Fig. 6a. (b) Detailed steady-state plastic dissipation zone for $h_t/R_0 = 0.5$ highlighting the two plastic dissipation zones A and C.

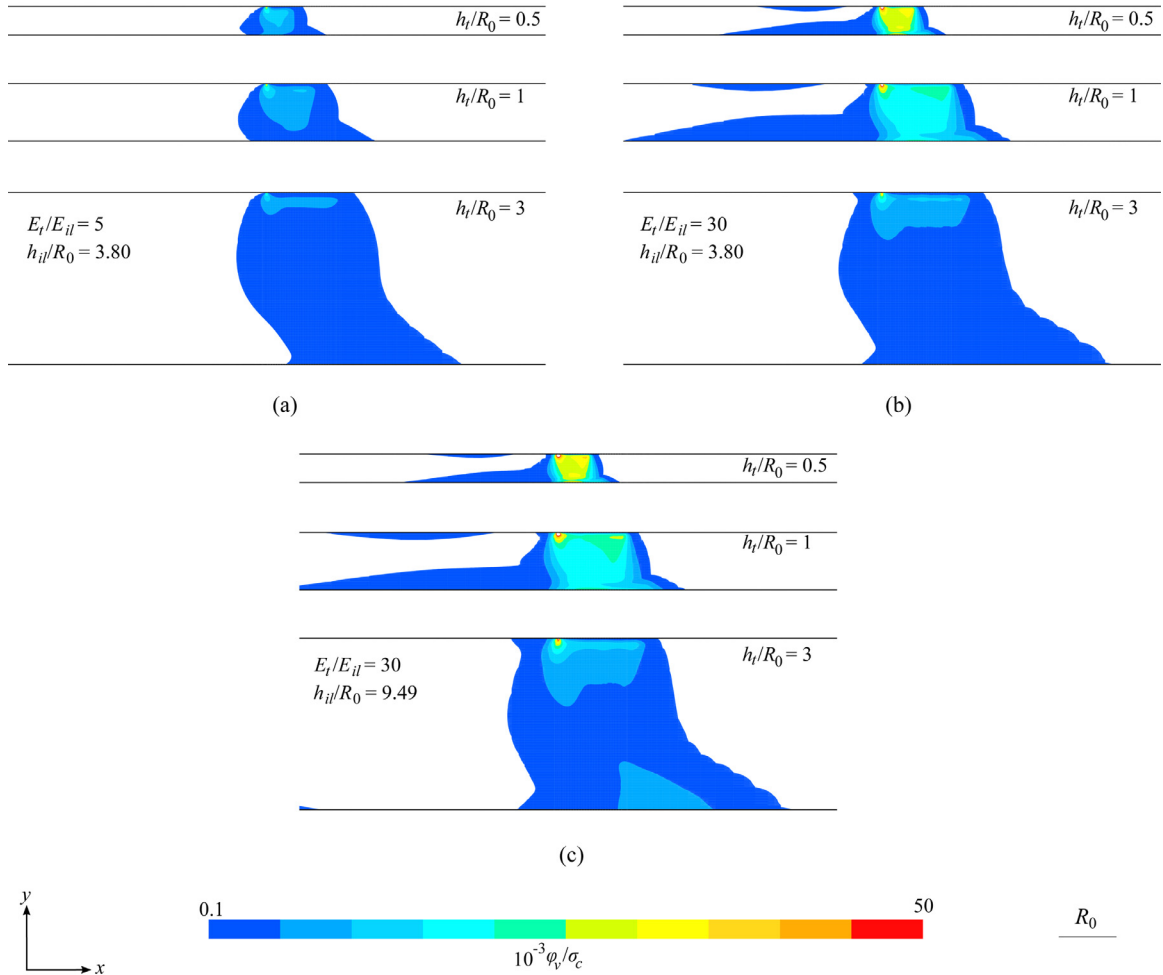


Fig. 11. Steady-state plastic dissipation zone in the thin layer in the presence of an elastic interlayer for three different values of h_t/R_0 , for (a) $E_t/E_{il} = 5$ and $h_{il}/R_0 = 3.80$, (b) $E_t/E_{il} = 30$ and $h_{il}/R_0 = 3.80$, (c) $E_t/E_i = 30$ and $h_{il}/R_0 = 9.49$. The corresponding evolution of $\Delta\phi_a/G_0$ is shown in Fig. 7.

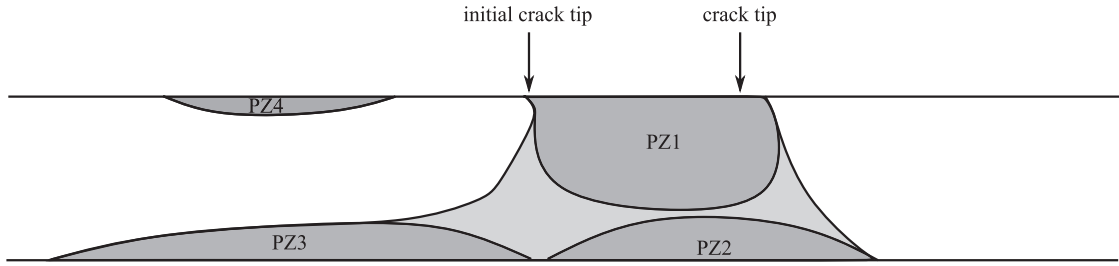


Fig. 12. Schematic representation of the four identified plastic dissipation zones in the thin layer for a system with an elastic interlayer.

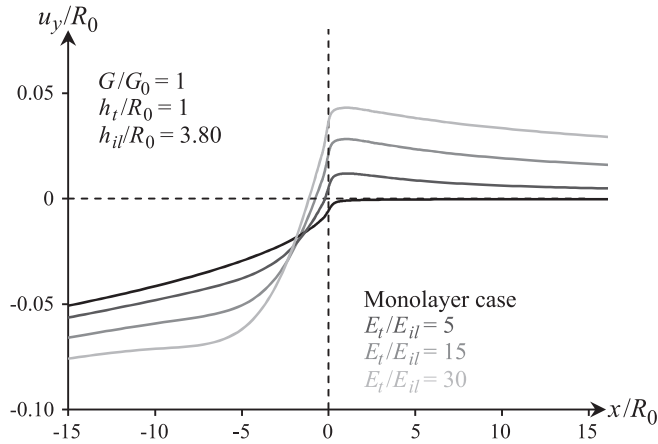


Fig. 13. Normal displacements along the mid thickness of the thin layer ($y = h_t/2$) normalized by R_0 for different E_t/E_{il} at $G = G_0$. The crack-tip is located at $x/R_0 = 0$. Other parameters are the ones from Fig. 6.

- at the crack face of the thin layer, behind the crack tip (PZ4).

PZ1 and PZ2 seem to be similar to PZA and PZC. This particular point is addressed later. While PZ4 is disconnected from the other plastic zones, PZ1, PZ2 and PZ3 are connected in most cases. It appears that the development of these plastic zones is not related to a single parameter, but rather to a combination of h_t/R_0 , E_t/E_{il} and h_{il}/R_0 . Most of the energy dissipation takes place in PZ1 and PZ2. Increasing h_t/R_0 increases the size of PZ1 while it decreases the intensity of the associated dissipation. This is the root cause of the evolution of G_{ss}/G_0 as a function of h_t/R_0 illustrated in Fig. 7. Increasing E_t/E_{il} and h_{il}/R_0 magnifies this phenomenon as illustrated in Fig. 11.

This change in plastic zones compared to the monolayer case is related to deviations from the linear elastic fracture mechanics (LEFM) solutions induced by the presence of the compliant interlayer. As shown in Fig. 13, the profile of normal displacement at the mid thickness of the thin layer $u_y = f(x)$ deviates significantly from the expected mode I LEFM profile (i.e., the monolayer case) when the interlayer is added. This is due to the asymmetry in stiffness between the upper and the lower part of the system which impacts the way the applied far-field displacements are transferred to the crack line, as schematized in Fig. 14. The resulting gradients in the $u_y = f(x)$ profile at mid-thickness of the thin layer generates the bending of this layer in the vicinity of the crack tip, subsequently giving rise to horizontal normal stress σ_{xx} concentrations as denoted from “1” to “4” in Fig. 14. Depending on the stiffness asymmetry and on the loading, these normal stresses govern the onset of plasticity in the thin layer: the stress concentration zones 1 to 4 schematized in Fig. 14 are responsible for the plastic zones PZ1 to PZ4, respectively, that were discussed previously (Fig. 12). The interaction between the vertical normal stress concentration under the crack tip, denoted as zone 5 on Fig. 14, and zone 1 and, for low enough h_t/R_0 , zone 2, leads to an increase of the von Mises stress at these locations. Thus, more energy is dissipated in zones PZ1 and PZ2 compared to PZ3 and PZ4. It follows that while they share the same locations and a similar dependence on h_t/R_0 , the plastic dissipation zones PZ1 and PZ2 in Fig. 12 cannot be identified with PZA and PZC, respectively (Fig. 10b).

The analysis of the effect of E_t/E_{il} and h_{il}/R_0 on the energy dissipation is straightforward, since these two parameters impact the stiffness of the lower half of the model. The toughness dependence on h_t/R_0 is affected by two competing phenomena. Decreasing h_t/R_0 leads to a decrease of the stiffness of the thin layer which is thus more prone to bending, thus more energy should be dissipated. However, a low h_t/R_0 value means that the volume of material available for plastic dissipation remains limited, which lowers the total amount of energy that can be effectively dissipated. There is thus an optimum h_t/R_0 for which the plastic dissipation is maximized. Increasing h_t/R_0 above this maximum reduces the deviations

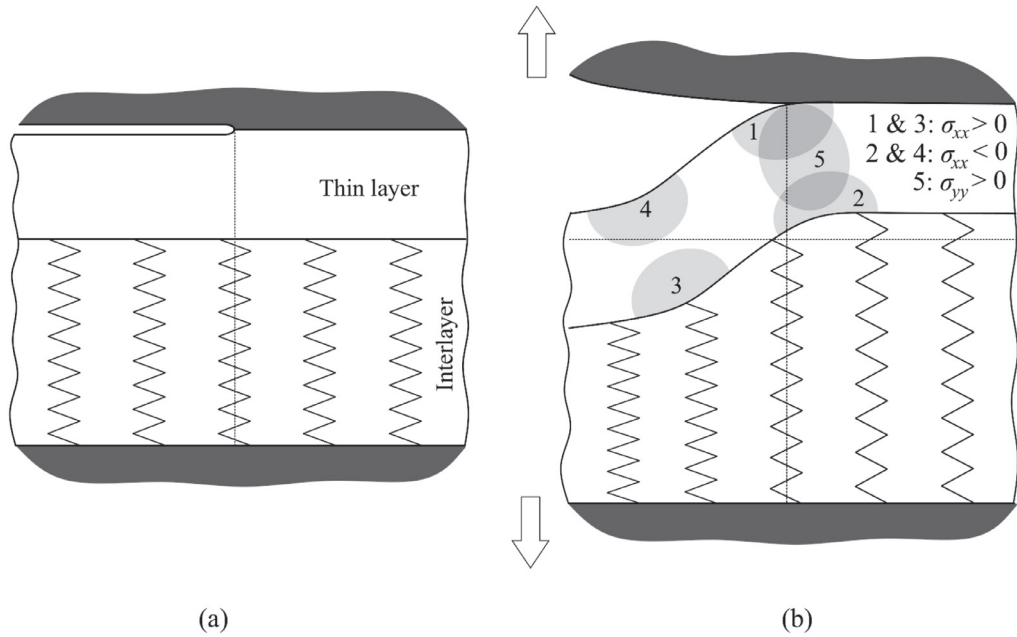


Fig. 14. Schematic representation of the multilayer, where the interlayer is represented by elastic springs, (a) prior to any crack opening and (b) under loading. Normal stress concentrations in the thin layer, resulting from a bending component, are highlighted.

from the LEFM solution, and the system behavior tends toward to the monolayer case, such that $\Delta\varphi_a/G_0 \rightarrow 0$ for large values of h_t/R_0 .

Increasing parameters E_s/E_t and σ_c/σ_{0_t} implies that a higher energy-release rate must be applied to advance the crack, therefore the thin film experiences more bending and $\Delta\varphi_a/G_0$ increases. Furthermore, the confinement of plasticity occurs for higher values of h_t/R_0 . Consequently, the maximum value for $\Delta\varphi_a/G_0$ is reached for larger h_t/R_0 .

A final remark on the influence of A_0/R_0 should be made. This parameter prescribes the displacement field applied at the edges of the crack faces, and therefore controls the magnitude of the deviation of the normal displacements from the LEFM solution. This effect is however of secondary importance: for $h_t/R_0 = 1$, $E_t/E_{il} = 30$ and $h_{il}/R_0 = 3.80$, values of G_{ss}/G_0 are found as 4.70, 4.80 and 5.0 for $A_0/R_0 = 1250, 938$ and 625, respectively.

4.2.3. Elastoplastic interlayer effect

Fig. 15 depicts the steady-state plastic dissipation zones in the thin layer and interlayer corresponding to the calculations addressed in Fig. 7 for three different h_t/R_0 . For the sake of comparison, Fig. 11c gives the corresponding steady-state plastic dissipation zone for $\sigma_{0_{il}}/E_{il} \rightarrow \infty$.

Three observations can be made from Figs. 15 and 11c. Decreasing the magnitude of $\sigma_{0_{il}}/E_{il}$ increases the interlayer plastic zone size. For $\sigma_{0_{il}}/E_{il} = 0.025$ (Fig. 15a), plasticity occurs over the entire thickness of the interlayer and extends well ahead of the crack tip, while it is mainly located directly under the crack tip for $\sigma_{0_{il}}/E_{il} = 0.05$ (Fig. 15b). For both cases, the plastic dissipation is at its highest in a zone located at the interface between the two layers. The magnitude of the plastic dissipation as well as the size of this zone tend to decrease with increasing h_t/R_0 . Finally, it appears that the plastic dissipation in the thin layer itself tends to increase with decreasing $\sigma_{0_{il}}/E_{il}$, and particularly for low values of h_t/R_0 .

The plasticity in the interlayer has two origins with a dependence on $\sigma_{0_{il}}/E_{il}$. The first origin is the interaction between the crack-tip stress field and the interlayer, which is directly related to h_t/R_0 and $\sigma_{0_{il}}/E_{il}$. Increasing E_s/E_t and σ_c/σ_{0_t} enhances the size and the magnitude of the crack-tip stress field, leading to more plasticity in the interlayer. This mechanism was already highlighted by Bertholet et al. (2007) and Wei and Hutchinson (1999) and is responsible for the plastic dissipation in the interlayer when $\sigma_{0_{il}}/E_{il} = 0.05$. The second origin for the plasticity in the interlayer is the normal tension that takes place in the interlayer ahead of the crack tip in the case of a compliant interlayer (Fig. 14). A yield strength of $\sigma_{0_{il}}/E_{il} = 0.025$ is low enough such that plastic strains in the interlayer can be induced through this tensile loading contribution only. This explains the large plastic dissipation zone ahead of the crack tip in Fig. 15a. From these two mechanisms, the toughening effect of increasing h_{il}/R_0 is similar to the effect of h_t/R_0 on the bond toughness in the monolayer case, i.e., a larger material volume is available for plastic dissipation. The increase of the plastic dissipation in the thin layer is an indirect consequence of the development of plasticity in the interlayer. Indeed, the values of $\sigma_{0_{il}}/E_{il}$ and N_{il} are such that after the onset of plasticity, further plastic strains can develop at relatively low stress levels. Thus, some of the applied remote energy release rate is dissipated through plastic deformation in the interlayer. As a consequence, a higher

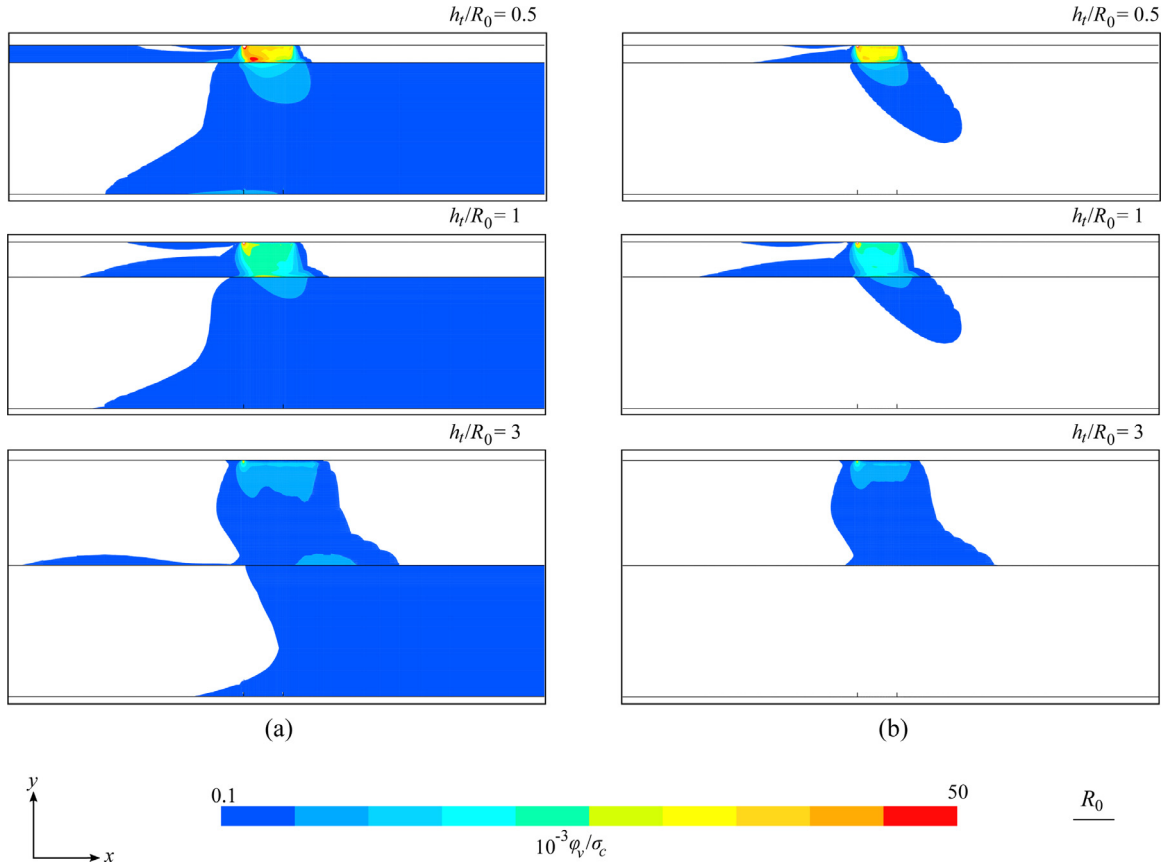


Fig. 15. Steady-state plastic dissipation zones corresponding the results from Fig. 6, for three different values of h_t/R_0 . (a) $\sigma_{0h}/E_{0l} = 0.025$, (b) $\sigma_{0h}/E_{0l} = 0.05$. Other parameters are $E_t/E_{0l} = 30$, $h_{0l}/R_0 = 3.80$, $E_s/E = 1$ and $\sigma_c/\sigma_0 = 4$.

remote energy release rate must be applied to advance the crack, which in turn leads to a more intense bending of the thin layer and thus an increase in the plastic dissipation in this layer, following the mechanisms explained in Section 4.2.2.

5. Experimental results and comparison with simulations

5.1. Measurement of the mode I interfacial toughness

Fig. 16 shows the evolution of the measured interface toughness G_c as a function of the Cu layer thickness h_t as extracted using Eqs. (1) and (2). A sharp drop in toughness occurs between $h_t = 0.5 \mu\text{m}$ and $1 \mu\text{m}$, then G_c decreases linearly with h_t .

Experimentally, the measured interface toughness G_c is the sum of the bonding energy G_0 , of the plastic energy dissipation φ , and of the energy contribution associated to the residual stresses in the layers G_R . Assuming that the plastic dissipation in the substrates is negligible, $G_0 + \varphi = G_c - G_R$. These experimental results can therefore be compared to the parametric simulations, provided a reasonable estimate can be found for G_R .

5.2. Quantification of the energy contribution from residual stresses

For a film that fully relaxes the stresses over its entire thickness during decohesion, the energy contribution of the residual stresses in the copper film G_R is given by Hutchinson and Suo (1991):

$$G_R = \int \frac{\sigma_R^2(h_t)}{2E_t(1-\nu_t^2)} dh_t = \frac{\sigma_R^2 h_t}{2E_t(1-\nu_t^2)}. \quad (18)$$

Experimentally, however, the Cu layer is not freestanding after delamination as it remains bonded to the adhesive film. Furthermore, there is no evidence that the film relaxes over its complete thickness, some elastic energy being stored in the crack wake. Thus, the real value of G_R is only a fraction of the expression given in Eq. (18), which represents an upper bound of the energy associated to the residual stresses.

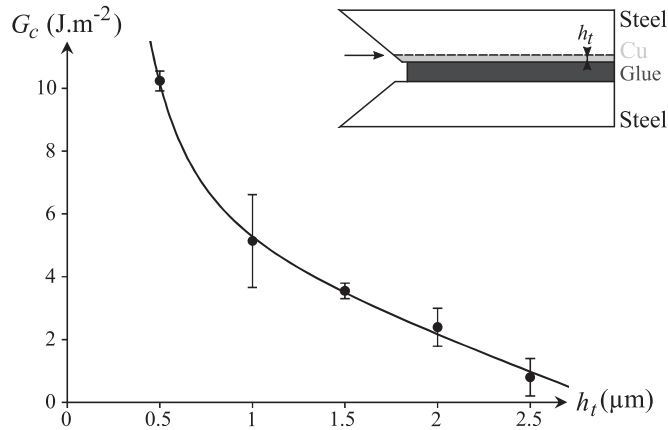


Fig. 16. Variation of the measured interface toughness as a function of the Cu film thickness.

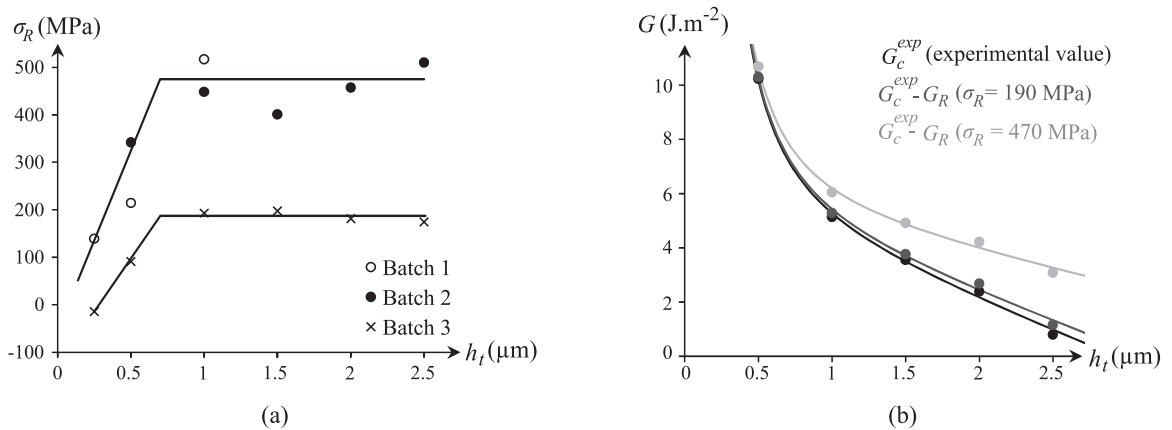


Fig. 17. (a) Evolution of the average residual stress in the copper film with the thickness, (b) Corresponding effect of the residual stress on the interface toughness. For more clarity, the standard deviations are not shown.

Fig. 17a summarizes the effect of the thickness h_t on the residual stress measured in the Cu layers. While there are considerable differences between the results from batches 1 and 2 on the one hand and from batch 3 on the other hand, in each case the stress increases linearly with thickness up to $1\ \mu\text{m}$ and then remains constant. The average value of the residual stress for thicknesses larger or equal to $1\ \mu\text{m}$ is $475\ \text{MPa}$ for batches 1 and 2, and $190\ \text{MPa}$ for batch 3. The determination of the origin of this deviation is beyond the scope of this study and may be related to different partial pressure of oxygen in the deposition chamber (Streppe, 2010). Fig. 17b shows the resulting value of $G_c - G_R$ for thickness-independent values of $\sigma_R = 190\ \text{MPa}$ and $470\ \text{MPa}$. The variation of G with respect to $\sigma_R = 190\ \text{MPa}$ can be considered as negligible. Conversely, a residual stress of $\sigma_R = 470\ \text{MPa}$ has a large effect on $G_c - G_R$, especially for larger thicknesses. In all cases, the general evolution of the interface toughness with the thickness remains the same: a sharp drop between 0.5 and $1\ \mu\text{m}$ followed by a linear decrease.

5.3. Comparison with the numerical simulations

Additional numerical simulations were performed to assess the toughening effect of the elastic mismatch between the Cu layer and the adhesive. The Cu film is identified with the thin film and the adhesive with the interlayer in Fig. 4a. For the reasons outlined in Section 3.5, these simulations do not allow to perform direct quantitative comparisons with the experimental results. Instead, the purpose here is to compare the trend of the evolution of G_{ss} with h_t for parameters with respect to the experimental trend.

Realistic values were taken for the mechanical properties of the constituents of the multilayer (Table 3). The yield strength dependence on the Cu film thickness was not taken into account, as the yield strength was reported to remain constant for copper films thicker than $1\ \mu\text{m}$, with values between $200\ \text{MPa}$ and $400\ \text{MPa}$ (Nicola et al., 2006; Xiang et al., 2006, 2001; Yu and Spaepen, 2004). Here, a yield strength σ_0 equal to $220\ \text{MPa}$ is assumed.

Table 3

Mechanical parameters selected for the steel substrate, the Cu layer and the adhesive for the experimental system.

	Stainless steel (substrate, $i = s$)	Copper (thin layer, $i = t$)	Adhesive (interlayer, $i = il$)
E_i (GPa)	190	110	3
ν_i	0.3	0.3	0.3
σ_{0i} (MPa)	–	220	20

Table 4

Non-dimensional parameters of Eq. (9).

σ_{0il}/E_t	N_t	σ_{0il}/E_{il}	N_{il}	E_s/E_t	E_t/E_{il}	ν	h_{il}/R_0	A_0/R_0	σ_c/σ_{0t}	δ_c/δ_e
0.002	0.1	0.007	0.1	1.7	36.7	0.3	20	5000	3.5	0.01

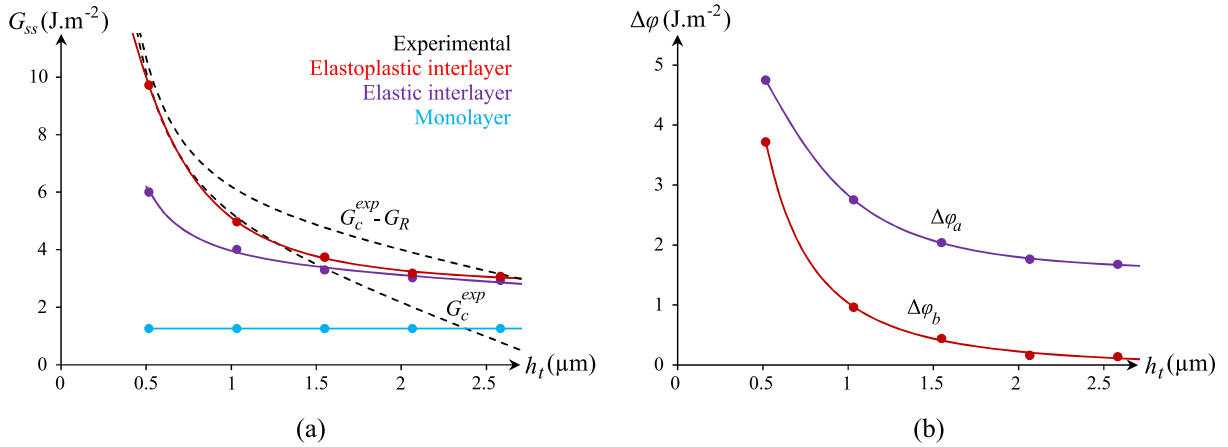


Fig. 18. (a) Comparison between numerical simulations and experimental results. The dashed lines represent the experimental trends with and without the effect of the residual stress ($\sigma_R = 470$ MPa), (b) Extra dissipations due to the elasticity and to the plasticity in the interlayer $\Delta\varphi_a$ and $\Delta\varphi_b$.

The parameters related to the interface can only be qualitatively guessed. G_0 was fixed as equal to 0.75 J m^{-2} and σ_c was adjusted such as to reproduce the results for $h_t/R_0 = 0.5$. A value of $\sigma_c = 770$ MPa was found. These values are consistent with a weak interface strength between the Cu layer and the substrate. This results in a reference plastic zone size $R_0 \sim 0.25 \mu\text{m}$. Since the copper film thickness experimentally varies between 0.5 and $2.5 \mu\text{m}$, the corresponding non-dimensional thickness h_t/R_0 varies between 2 and 10 .

The FE mesh was modified in order to run new calculations corresponding to the range of interest for the parameters of this specific application. In order to reduce the number of elements per calculations, the ratio R_0/d_0 was set to 50 , corresponding to a mesh resolution of $\delta_c/d_0 = 0.37$. The thickness of the adhesive h_{il} was set to $5 \mu\text{m}$ (i.e., $h_{il}/R_0 = 20$). This value is most probably underestimated but was chosen for computational reasons, as higher values of h_{il}/R_0 would result in a large total thickness h in the model. Finally, $A_0/(h_t + h_{il})$ varies between 50 and 100 for a constant $A_0/R_0 = 2000$. Note that the resulting value of $A_0 \sim 0.5 \text{ mm}$ is larger than the arm thickness $h_a = 0.4 \text{ mm}$. The non-dimensional parameters of Eq. (9) are summarized in Table 4.

The comparison between the simulations results and the experimental results is given in Fig. 18a. Despite numerous uncertainties, the general trend of the variation of G_{ss} with h_t agrees well with the experimental results. The extra dissipation associated to the elastoplastic or only elastic deformation of the interlayer is shown in Fig. 18b. The higher toughness for $h_t = 0.5 \mu\text{m}$ is clearly the result of significant amount of plastic dissipation in the adhesive “interlayer”. For larger thickness, this contribution decreases and becomes negligible: most or all of the toughening arises from the elasticity of the interlayer. This is a direct consequence of the low value of σ_c and the large values of h_t/R_0 : the stress-field arising from the crack tip only interacts slightly with the interlayer, and the relatively large values of $\Delta\varphi_a$ are due to the large values of E_t/E_{il} and h_{il}/R_0 . This raises of course concerns regarding the experimental determination of G_c with test configurations involving a second substrate added for practical reasons.

6. Conclusion

The effect of the presence of an adjacent interlayer on the toughness of an interface between a thin layer and a substrate has been investigated numerically using a K -field finite element formalism. The interface toughness can be improved through two phenomena: (i) the generation of additional plastic zones in the thin layer due to a softer interlayer and (ii)

the development of plasticity in the interlayer. This first phenomenon arises from the stiffness asymmetry on each side of the crack plane which leads to the bending of the thin layer, and is thus magnified by increasing the compliance and the thickness of the interlayer. An optimum toughness is found for a film thickness corresponding to a compromise between the available volume for plastic dissipation, which increases with increasing thickness, and the magnitude of the bending of the film, which increases with decreasing thickness. The second phenomenon is especially relevant for small layer thickness and low interlayer yield strength. The experimental dependence that was found between the interface toughness of a multilayer specimen and the thickness of a layer constituting this interface is consistent with a toughening induced by a ductile compliant interlayer. These results pave the way to further optimization of the interface reliability of a variety of multilayers. Some guidelines should be followed:

- (i) The interlayer must be softer than the thin layer, and/or the interlayer must exhibit a lower yield strength than the thin layer. These conditions ensure that the bending of the thin layer and/or the plasticity in the interlayer will occur during crack propagation. Even a slightly softer interlayer compared to the thin layer should yield a slight improvement of the interfacial toughness, which then increases with decreasing the Young's modulus of the interlayer.
- (ii) The total thickness of the thin layer and of the interlayer must be smaller than the K-dominated zone. Thus, a compromise has to be made regarding the thickness of the interlayer: a thick interlayer leads to a higher toughness, but a too thick interlayer may have no effect.
- (iii) The interlayer must exhibit a toughness higher than the weak interface of interest. Otherwise, the crack is susceptible to propagate through the interlayer. Similarly, the interfaces adjacent to the interlayer must be as tough as possible.

Finally, the present work shows that interface toughness measurements for thin films on substrate using methods that require the bonding of a top substrate (dummy substrate) such as DCB or four point bending tests must be analyzed with care as the glue layer may have a large effect on the interface toughness. The present model constitutes a way to quantify this extra amount of energy that must be subtracted from the measurement energy release rate to determine the true interface toughness. This is an issue that has not been sufficiently taken into account in the literature, with published results probably requiring some re-analysis.

Acknowledgments

The authors wish to thank the “Région Wallonne” for the financial support in the framework of the “Programme d'Excellence FLYCOAT” and of the FIRST DEI Programme with the project “JADHERE” (Convention 516122) jointly with the company ArcelorMittal.

Declarations of interest

None.

Appendix A

The coefficients ϕ , λ , $A(a)$ and $B(a)$ in Eq. (2) are as follows:

$$A(a) = \left[\frac{\sinh^2 \lambda c + \sin^2 \lambda c}{\sinh^2 \lambda c - \sin^2 \lambda c} \right] + 2a\lambda \left[\frac{\sinh \lambda c \cosh \lambda c - \sin \lambda c \cos \lambda c}{\sinh \lambda c \cosh \lambda c - \sin \lambda c \cos \lambda c} \right], \quad (\text{A.1})$$

$$B(a) = \left[\frac{\sinh \lambda c \cosh \lambda c + \sin \lambda c \cos \lambda c}{\sinh^2 \lambda c - \sin^2 \lambda c} \right] + a\lambda \left[\frac{\sinh^2 \lambda c + \sin^2 \lambda c}{\sinh^2 \lambda c - \sin^2 \lambda c} \right], \quad (\text{A.2})$$

$$\phi = \frac{2}{\lambda^3 h_a^3} \left[2\lambda^3 h_a^3 + 6\lambda^2 h_a^2 \left(\frac{\sinh \lambda c \cosh \lambda c - \sin \lambda c \cos \lambda c}{\sinh^2 \lambda c - \sin^2 \lambda c} \right) + 6\lambda h_a \left(\frac{\sinh^2 \lambda c + \sin^2 \lambda c}{\sinh^2 \lambda c - \sin^2 \lambda c} \right) + 3 \left(\frac{\sinh \lambda c \cosh \lambda c + \sin \lambda c \cos \lambda c}{\sinh^2 \lambda c - \sin^2 \lambda c} \right) \right], \quad (\text{A.3})$$

$$\lambda^4 = \frac{3k}{E_s b h_a^3}, \quad (\text{A.4})$$

where k is the stiffness of the spring model for the foundation, such that $k = 1.615 Eb/h_a$ (Li et al., 2004), and b is the width of the beam.

References

- Argon, A.S., Gupta, V., Landis, H.S., Cornie, J.A., 1989. Intrinsic toughness of interfaces between SiC coatings and substrates of Si or C fibre. *J. Mater. Sci.* 24, 1207–1218. doi:[10.1007/BF02397049](https://doi.org/10.1007/BF02397049).
- Bertholet, Y., Iker, F., Raskin, J.P., Pardoën, T., 2004. Steady-state measurement of wafer bonding cracking resistance. *Sens. Actuat. A Phys.* 110, 157–163. doi:[10.1016/j.sna.2003.09.004](https://doi.org/10.1016/j.sna.2003.09.004).
- Bertholet, Y., Olbrechts, B., Lejeune, B., Raskin, J.P., Pardoën, T., 2007. Molecular bonding aided by dissipative inter-layers. *Acta Mater.* 55, 473–479. doi:[10.1016/j.actamat.2006.08.036](https://doi.org/10.1016/j.actamat.2006.08.036).
- Brown, H.R., 1991. The adhesion between Polymers. *Annu. Rev. Mater. Sci.* 21, 463–489. doi:[10.1146/annurev.ms.21.080191.002335](https://doi.org/10.1146/annurev.ms.21.080191.002335).
- Bruyneel, M., Delsemme, J.P., Goupil, A.C., Jetteur, P., Lequesne, C., Naito, T., Urushiyama, Y., 2014. Damage modeling of laminated composites: validation of the intra-laminar law of SAMCEF at the coupon level for UD plies. In: *Proceedings of the ECCM16 - 16th European Conference on Composite Materials*. Seville, Spain.
- Charalambides, M., Kinloch, A.J., Wang, Y., Williams, J.G., 1992. On the analysis of mixed-mode failure. *Int. J. Fract.* 54, 269–291. doi:[10.1007/BF00035361](https://doi.org/10.1007/BF00035361).
- Cordisco, F.A., Zavattieri, P.D., Hector, L.G., Carlson, B.E., 2016. Mode I fracture along adhesively bonded sinusoidal interfaces. *Int. J. Solids Struct.* 83, 45–64. doi:[10.1016/j.ijsolstr.2015.12.028](https://doi.org/10.1016/j.ijsolstr.2015.12.028).
- Dauskardt, R.H., Lane, M., Ma, Q., Krishna, N., 1998. Adhesion and debonding of multi-layer thin film structures. *Eng. Fract. Mech.* 61, 141–162. doi:[10.1016/S0013-7944\(98\)00052-6](https://doi.org/10.1016/S0013-7944(98)00052-6).
- Dupont, S.R., Voroshazi, E., Heremans, P., Dauskardt, R.H., 2013. Adhesion properties of inverted polymer solarcells: processing and film structure parameters. *Org. Electron.* 14, 1262–1270. doi:[10.1016/j.orgel.2013.02.022](https://doi.org/10.1016/j.orgel.2013.02.022).
- Freund, L.B., Suresh, S., 2004. *Thin film materials: stress, Defect Formation and Surface Evolution*. Cambridge University Press, Cambridge.
- Gandhi, D.D., Lane, M., Zhou, Y., Singh, A.P., Nayak, S., Tisch, U., Eizenberg, M., Ramanath, G., 2007. Annealing-induced interfacial toughening using a molecular nanolayer. *Nature* 447, 299–302. doi:[10.1038/nature05826](https://doi.org/10.1038/nature05826).
- He, M.Y., Evans, A.G., Hutchinson, J.W., 1997. Convergent debonding of films and fibers. *Acta Mater.* 45, 3481–3489. doi:[10.1016/S1359-6454\(96\)00395-3](https://doi.org/10.1016/S1359-6454(96)00395-3).
- Huang, Z., Suo, Z., Xu, G., He, J., Prévost, J.H., Sukumar, N., 2005. Initiation and arrest of an interfacial crack in a four-point bend test. *Eng. Fract. Mech.* 72, 2584–2601. doi:[10.1016/j.engfracmech.2005.04.002](https://doi.org/10.1016/j.engfracmech.2005.04.002).
- Hughey, M.P., Morris, D.J., Cook, R.F., Bozeman, S.P., Kelly, B.L., Chakravarty, S.L.N., Harkens, D.P., Stearns, L.C., 2004. Four-point bend adhesion measurements of copper and permalloy systems. *Eng. Fract. Mech.* 71, 245–261. doi:[10.1016/S0013-7944\(03\)00100-0](https://doi.org/10.1016/S0013-7944(03)00100-0).
- Hutchinson, J.W., Suo, Z., 1991. Mixed mode cracking in layered materials. *Adv. Appl. Mech.* 29, 63–191. doi:[10.1016/S0065-2156\(08\)70164-9](https://doi.org/10.1016/S0065-2156(08)70164-9).
- Ikeda, T., Yamashita, A., Lee, D., Miyazaki, N., 2000. Failure of a ductile adhesive layer constrained by hard adherends. *J. Eng. Mater. Technol.* 122, 80. doi:[10.1115/1.482769](https://doi.org/10.1115/1.482769).
- Kanninen, M.F., 1973. An augmented double cantilever beam model for studying crack propagation and arrest. *Int. J. Fract.* 9, 83–92. doi:[10.1007/BF00035958](https://doi.org/10.1007/BF00035958).
- Kim, J.K., Cheon, T.H., Kim, S.H., Park, Y.B., 2012a. Interfacial adhesion energy of Ru-AIO thin film deposited by atomic layer deposition between Cu and SiO₂: effect of the composition of Ru-AIO thin film. *Jpn. J. Appl. Phys.* 51, 05EB04. doi:[10.1143/JJAP.51.05EB04](https://doi.org/10.1143/JJAP.51.05EB04).
- Kim, W.S., Yun, I.H., Lee, J.J., Jung, H.T., 2010. Evaluation of mechanical interlock effect on adhesion strength of polymermetal interfaces using micro-patterned surface topography. *Int. J. Adhes. Adhes.* 30, 408–417. doi:[10.1016/j.ijadhadh.2010.05.004](https://doi.org/10.1016/j.ijadhadh.2010.05.004).
- Kim, Y., Bulusu, A., Giordano, A.J., Marder, S.R., Dauskardt, R., Graham, S., 2012b. Experimental study of interfacial fracture toughness in a SiN_x/PMMA barrier film. *ACS Appl. Mater. Interfaces* 4, 6711–6719. doi:[10.1021/am301880y](https://doi.org/10.1021/am301880y).
- Kinloch, A.J., Shaw, S.J., 1981. The fracture resistance of a toughened epoxy adhesive. *J. Adhes.* 12, 59–77. doi:[10.1080/00218468108071189](https://doi.org/10.1080/00218468108071189).
- Ključar, L., Gonzalez, M., Vanstreels, K., Ivanković, A., Hecker, M., De Wolf, I., 2015. Effect of 4-point bending test procedure on crack propagation in thin film stacks. *Microelectron. Eng.* 137, 59–63. doi:[10.1016/j.mee.2014.09.006](https://doi.org/10.1016/j.mee.2014.09.006).
- Ladevèze, P., Allix, O., Douchin, B., Lévêque, D., 1998. A computational method for damage intensity prediction in a laminated composite structure. In: *Idelsohn, S., Oñate, E., Dvorkin, E. (Eds.), Computational Mechanics – New Trends and Applications*. CIMNE, Barcelona, Spain.
- Lane, M., Dauskardt, R.H., Krishna, N., Hashim, I., 2000a. Adhesion and reliability of copper interconnects with Ta and TaN barrier layers. *J. Mater. Res.* 15, 203–211. doi:[10.1557/JMR.2000.0033](https://doi.org/10.1557/JMR.2000.0033).
- Lane, M., Dauskardt, R.H., Vainchtein, A., Gao, H., 2000b. Plasticity contributions to interface adhesion in thin-film interconnect structures. *J. Mater. Res.* 15, 2758–2769. doi:[10.1557/JMR.2000.0395](https://doi.org/10.1557/JMR.2000.0395).
- Larsson, M.P., Syms, R.R.A., Wojcik, A.G., 2005. Improved adhesion in hybrid Si-polymer MEMS via micromechanical interlocking. *J. Micromech. Microeng.* 15, 2074–2082. doi:[10.1088/0960-1317/15/11/012](https://doi.org/10.1088/0960-1317/15/11/012).
- Lee, I., Kim, S., Yun, J., Park, I., Kim, T.S., 2012. Interfacial toughening of solution processed Ag nanoparticle thin films by organic residuals. *Nanotechnology* 23, 485704. doi:[10.1088/0957-4484/23/48/485704](https://doi.org/10.1088/0957-4484/23/48/485704).
- Lemons, A.M., Kershen, K., Bennett, J., Pfeifer, K., Sun, Y.-M., White, J.M., Ekerdt, J.G., 2002. Adhesion of Cu and low-k dielectric thin films with tungsten carbide. *J. Mater. Res.* 17, 1320–1328. doi:[10.1557/JMR.2002.0197](https://doi.org/10.1557/JMR.2002.0197).
- Li, S., Wang, J., Thouless, M.D., 2004. The effects of shear on delamination in layered materials. *J. Mech. Phys. Solids* 52, 193–214. doi:[10.1016/S0022-5096\(03\)00070-X](https://doi.org/10.1016/S0022-5096(03)00070-X).
- Maloney, K., Fleck, N., 2019. Toughening strategies in adhesive joints. *Int. J. Solids Struct.* 158, 66–75. doi:[10.1016/j.ijsolstr.2018.08.028](https://doi.org/10.1016/j.ijsolstr.2018.08.028).
- Martiny, P., Lani, F., Kinloch, A.J., Pardoën, T., 2012. A multiscale parametric study of mode I fracture in metal-to-metal low-toughness adhesive joints. *Int. J. Fract.* 173, 105–133. doi:[10.1007/s10704-011-9667-x](https://doi.org/10.1007/s10704-011-9667-x).
- Matsuda, Y., Ryu, I., King, S.W., Bielefeld, J., Dauskardt, R.H., 2014. Toughening thin-film structures with ceramic-like amorphous silicon carbide films. *Small* 10, 253–257. doi:[10.1002/smll.201300130](https://doi.org/10.1002/smll.201300130).
- Navarro, E., Bréchet, Y., Moreau, R., Pardoën, T., Raskin, J.-P., Barthelemy, A., Radu, I., 2013. Direct silicon bonding dynamics: a coupled fluid/structure analysis. *Appl. Phys. Lett.* 103, 034104. doi:[10.1063/1.4813312](https://doi.org/10.1063/1.4813312).
- Nicola, L., Xiang, Y., Vlassak, J.J., Van der Giessen, E., Needleman, A., 2006. Plastic deformation of freestanding thin films: experiments and modeling. *J. Mech. Phys. Solids* 54, 2089–2110. doi:[10.1016/j.jmps.2006.04.005](https://doi.org/10.1016/j.jmps.2006.04.005).
- Olbrechts, B., Lejeune, B., Bertholet, Y., Pardoën, T., Raskin, J.-P., 2006. Direct wafer bonding enhanced by ductile layers inserted near the interface, in: *ECS transactions*. ECS 279–289. doi:[10.1149/1.2357078](https://doi.org/10.1149/1.2357078).
- Pardoën, T., Ferracin, T., Landis, C.M., Delannay, F., 2005. Constraint effects in adhesive joint fracture. *J. Mech. Phys. Solids* 53, 1951–1983. doi:[10.1016/j.jmps.2005.04.009](https://doi.org/10.1016/j.jmps.2005.04.009).
- Stoney, G.G., 1909. The tension of metallic films deposited by Electrolysis, in: *proceedings of the royal society A: mathematical. Phys. Eng. Sci. R. Soc.* 172–175. doi:[10.1098/rspa.1909.0021](https://doi.org/10.1098/rspa.1909.0021).
- Streppe, F., 2010. *Adhesion of Thin Films On Steel and Separation of the Energy Contributions*. Université Catholique de Louvain.
- Strohband, S., Dauskardt, R.H., 2003. Interface separation in residually-stressed thin-film structures. *Interface Sci.* 11, 309–317. doi:[10.1023/A:1025196306794](https://doi.org/10.1023/A:1025196306794).
- Tvergaard, V., 2003. Influence of plasticity on interface toughness in a layered solid with residual stresses. *Int. J. Solids Struct.* 40, 5769–5779. doi:[10.1016/S0020-7683\(03\)00342-1](https://doi.org/10.1016/S0020-7683(03)00342-1).
- Tvergaard, V., Hutchinson, J.W., 1996. On the toughness of ductile adhesive joints. *J. Mech. Phys. Solids* 44, 789–800. doi:[10.1016/0022-5096\(96\)00011-7](https://doi.org/10.1016/0022-5096(96)00011-7).
- Tvergaard, V., Hutchinson, J.W., 1994. Toughness of an interface along a thin ductile layer joining elastic solids. *Philos. Mag. A* 70, 641–656. doi:[10.1080/01418619408242253](https://doi.org/10.1080/01418619408242253).
- Tvergaard, V., Hutchinson, J.W., 1993. The influence of plasticity on mixed mode interface toughness. *J. Mech. Phys. Solids* 41, 1119–1135. doi:[10.1016/0022-5096\(93\)90057-M](https://doi.org/10.1016/0022-5096(93)90057-M).

- Tvergaard, V., Hutchinson, J.W., 1992. The relation between crack growth resistance and fracture process parameters in elastic-plastic solids. *J. Mech. Phys. Solids* 40, 1377–1397. doi:[10.1016/0022-5096\(92\)90020-3](https://doi.org/10.1016/0022-5096(92)90020-3).
- Wei, Y., Hutchinson, J.W., 1999. Models of interface separation accompanied by plastic dissipation at multiple scales. *Int. J. Fract.* 95, 1–17. doi:[10.1023/A:1018627712739](https://doi.org/10.1023/A:1018627712739).
- Xiang, Y., Chen, X., Vlassak, J.J., 2001. The mechanical properties of electroplated Cu thin films measured by means of the bulge test technique. In: *MRS Proc.*, 695. L4.9.1 doi: [10.1557/PROC-695-L4.9.1](https://doi.org/10.1557/PROC-695-L4.9.1).
- Xiang, Y., Tsui, T.Y., Vlassak, J.J., 2006. The mechanical properties of freestanding electroplated Cu thin films. *J. Mater. Res.* 21, 1607–1618. doi:[10.1557/jmr.2006.0195](https://doi.org/10.1557/jmr.2006.0195).
- Yu, D., Spaepen, F., 2004. The yield strength of thin copper films on Kapton. *J. Appl. Phys.* 95, 2991–2997. doi:[10.1063/1.1644634](https://doi.org/10.1063/1.1644634).